Volume 53
Number 40
28 October 2024
Pages 16425-16760

Dalton Transactions

An international journal of inorganic chemistry

rsc.li/dalton

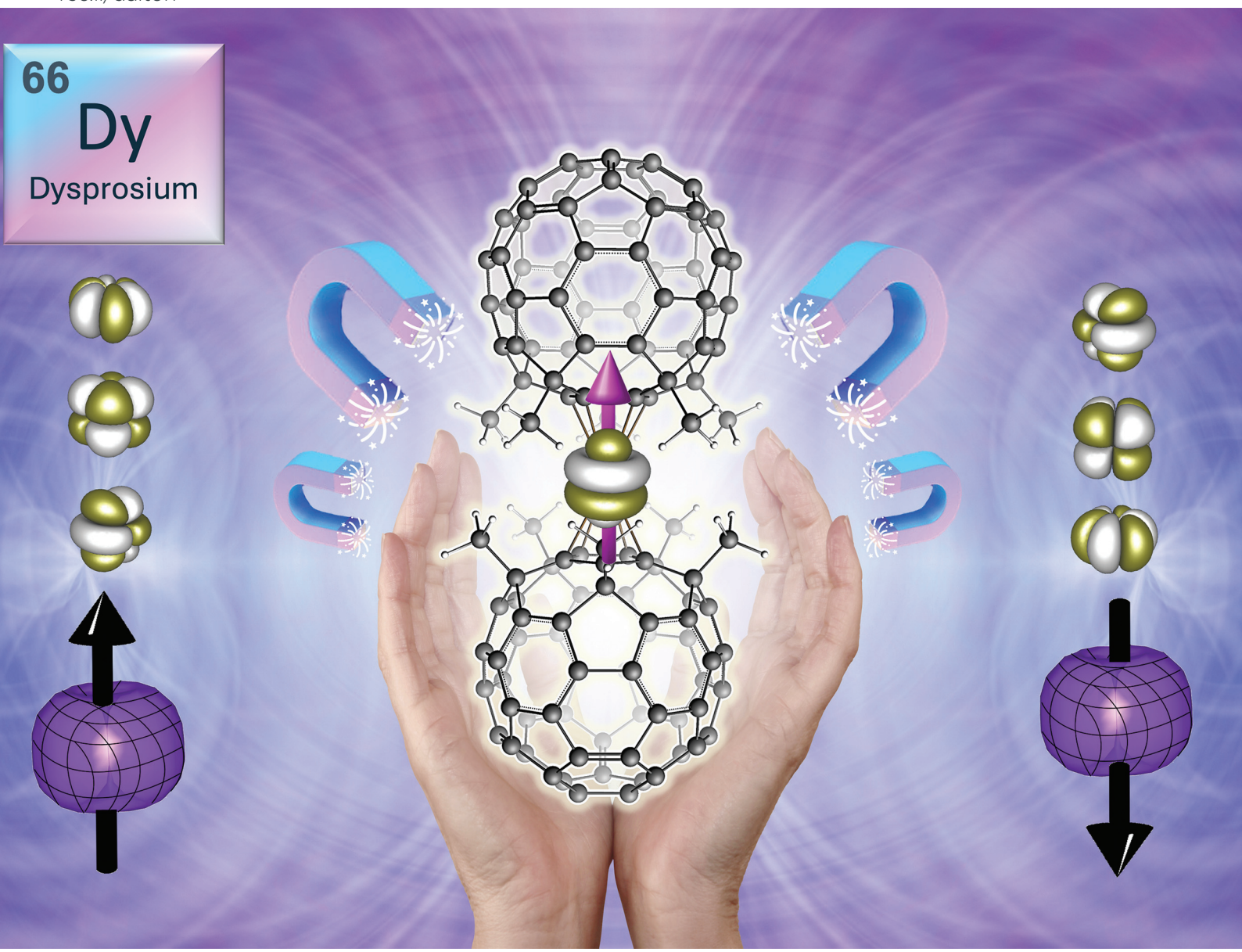

ISSN 1477-9226

ROYAL SOCIETY OF CHEMISTRY

PAPER

Kusum Kumari and Saurabh Kumar Singh
Substituted fullerenes as a promising capping ligand towards stabilization of exohedral Dy(III) based single-ion magnets: a theoretical study

Dalton Transactions

ROYAL SOCIETY OF CHEMISTRY

PAPER

View Article Online
View Journal | View Issue

Cite this: *Dalton Trans.*, 2024, **53**, 16495

Substituted fullerenes as a promising capping ligand towards stabilization of exohedral Dy(III) based single-ion magnets: a theoretical study†

Kusum Kumari and Saurabh Kumar Singh *

Organometallic dysprosocenium-based molecular magnets are the forefront runners in offering giant magnetic anisotropy and blocking temperatures close to the boiling point of liquid nitrogen. Attaining linearity in the organometallic dysprosocenium complexes is the key to generating giant magnetic anisotropy and blocking barriers. In the present study, we have unravelled the coordination ability of the substituted fullerene $(C_{55}X_5)^-$ (where X = CCH_3, B, and N) generated by fencing around the five-membered ring of fullerene towards stabilizing a new family of exohedral dysprosium organometallic complexes showcasing giant magnetic anisotropy and blockade barriers. Eight exohedral mononuclear dysprosium organometallic complexes, namely $[Dy(\eta^5\text{-}C_{55}X_5)(\eta^4\text{-}C_4H_4)]$ (**1**), $[Dy(\eta^5\text{-}C_{55}X_5)(\eta^5\text{-}Cp)]^+$ (**2**), $[Dy(\eta^5\text{-}C_{55}X_5)(\eta^5\text{-}Cp^*)]^+$ (**3**), $[Dy(\eta^5\text{-}C_{55}X_5)(\eta^6\text{-}C_6H_6)]^{2+}$ (**4**), $[Dy(\eta^5\text{-}C_{55}X_5)(\eta^8\text{-}C_8H_8)]$ (**5**), $[Dy(\eta^5\text{-}C_{55}X_5)_2]^+$ (**6**) (where X = CCH_3), $[Dy(\eta^5\text{-}C_{55}B_5)_2]^+$ (**7**) and $[Dy(\eta^5\text{-}C_{55}N_5)_2]^+$ (**8**), were studied using scalar relativistic density functional theory (SR-DFT) and the complete active space self-consistent field (CASSCF) methodology to shed light on the structure, stability, bonding and single-ion magnetic properties. SR-DFT calculations predict complexes **1–8** to be highly stable, with a strictly linear geometry around the Dy(III) ion in complexes **6–8**. Energy Decomposition Analysis (EDA) predicts the following order for interaction energy (ΔE_{int} value): **5** > **1** > **2** ≈ **3** > **6** > **7** > **8** > **4**, with sizable 4f-ligand covalency in all the complexes. CASSCF calculations on complexes **1–8** predict stabilization of m_J $|\pm15/2\rangle$ as the ground state for all the complexes except for **5**, with the following trend in the U_{cal} values: **6** (1573 cm^{-1}) ≈ **3** (1569 cm^{-1}) > **1** (1538 cm^{-1}) > **8** (1347 cm^{-1}) > **2** (1305 cm^{-1}) > **7** (1284 cm^{-1}) > **4** (1125 cm^{-1}) > **5** (108 cm^{-1}). *Ab initio* ligand field theory (AILFT) analysis provides a rationale for U_{cal} ordering, where π-type 4f-ligand interactions in complexes **1–4** and **6–8** offer giant barrier height while the large $(C_8H_8)^{2-}$ rings generate δ-type interaction in **5**, which diminishes the axiality in the ligand field. Our detailed finding suggests that the exohedral organometallic dysprosocenium complexes are more linear compared to bent $[DyCp^*_2]^+$ cations and display a giant barrier height exceeding 1500 cm^{-1} with negligible quantum tunnelling of magnetization (QTM) – a new approach to design highly anisotropic dysprosium organometallic complexes.

Received 20th July 2024,
Accepted 26th August 2024

DOI: 10.1039/d4dt02090a

rsc.li/dalton

Introduction

Single Molecule Magnets (SMMs) have garnered significant attention in the scientific community over the past few decades due to their unique property of displaying molecular hysteresis stemming from the intrinsic barrier height for magnetization reversal.[1–5] As a result, these molecules hold immense promise for various technological applications, including molecular qubits,[6–8] high-density data storage devices,[9–12] and spintronics.[13,14] Extensive research spanning over three decades on designing molecule-based magnets has identified that mononuclear transition metal[15] and lanthanide complexes[1] are much more appealing candidates for designing highly anisotropic SMMs compared to polynuclear complexes,[16] thanks to the giant and tuneable magnetic anisotropy at the mononuclear level.[17] Due to the unquenched orbital angular momentum associated with 4f-ions, the trivalent lanthanide ions naturally become more appealing candidates for designing SMMs with giant barrier heights.[1] In particular, trivalent Dy(III) ions are highly efficient in stabilizing SMMs with a giant magnetic relaxation barrier >2000 K and blocking temperatures close to the boiling point of liquid nitrogen.[18] To achieve Ising type anisotropy in Dy(III) complexes, a robust axial ligand field and extremely weak/negligible equatorial

Computational Inorganic Chemistry Group, Department of Chemistry, Indian Institute of Technology Hyderabad, Kandi, Sangareddy, Telangana-502284, India. E-mail: sksingh@chy.iith.ac.in

† Electronic supplementary information (ESI) available. See DOI: https://doi.org/10.1039/d4dt02090a

ligand field around a Dy(III) ion is required to stabilize the largest m_J $|\pm 15/2\rangle$ as the ground state.[19–24] In this context, organometallic sandwiched $[DyCp_2]^+$ based cations show remarkable SMM properties, as the strong π-type interaction between the 4f orbitals of Dy(III) and π-lobes of the monoanionic cyclopentadienyl (Cp) ligands generates a strong axial ligand field which generates a giant barrier height for magnetization reversal.[18,25–27] Mills and co-workers have reported the $[Dy(Cp^{ttt})_2][B(C_6F_5)_4]$ (where Cp^{ttt} = $(C_5H_2{}^tBu_3$-1,2,4) and ^tBu = $C(CH_3)_3$) complex where the ∠Cp–Dy–Cp bond angle is reported to be 152.6° and displays a magnetic hysteresis at 60 K.[25] One common strategy to maximize the anisotropy in the $[DyCp_2]^+$ family of complexes is to achieve strict linearity around the Dy(III) ion, *i.e.* maintaining the ∠Cp–Dy–Cp bond angle at ~180°. Bulking up the Cp ligand is a popular approach where the enhanced steric interaction can offer linearity in the ∠Cp–Dy–Cp bond angle, resulting in a large barrier height. Numerous attempts have been made to isolate linear dysprosocenium cations; however, the maximum ∠Cp–Dy–Cp bond angle of 162.5° is observed in the groundbreaking report of the $[DyCp^{ip5}Cp^*][B(C_6F_5)_4]$ (where Cp^{ip5} = penta-iso-propylcyclopentadienyl; Cp* = pentamethylcyclopentadienyl) complex showing the largest T_B value of 80 K.[18] Another promising strategy is introducing heteroatoms (B, Ge, P, N, and Pb) to functionalize the Cp rings,[26,27,27,28] which is also a key to increasing the barrier height as both the electrostatics and covalency can help in tweaking the magnetic anisotropy. Some notable work includes the report on the $[Dy(BC_4Ph_5)_2]^-$ complex,[26] where boron substitution in the Cp ring generates stronger electrostatics resulting in a high T_B value of 65 K. Another key example is the report on $[(Cp^{iPr5})Dy(Cp^{PEt4})]^+$, where the presence of Cp^{PEt4} (tetraethylphospholyl) ligands results in a high T_B value of 70 K for this complex.[28] As an alternative to $(Cp)^-$ ligands, computational observations predict that the cyclobutadiene dianion $(C_4H_4)^{2-}$ ligands[29] are even more promising to achieve a large barrier height; however, these $[Dy(C_4H_4)_2]^-$ family complexes are yet to be synthesized.[30] Other strategies include synthesizing highly symmetric environment Dy(III) complexes with axially compressed Dy–ligand bonds over the equatorial Dy–ligand bonds, resulting in giant magnetic anisotropy.[21,22,31–36] Numerous homoleptic and heteroleptic lanthanide sandwich complexes with larger rings have been reported in the literature, and a near linear geometry around the Dy(III) ion displays weak SMM behaviour.[37–39] The larger ring size introduces adverse ligand field effects, generating an unfavourable equatorial ligand field, which diminishes the SMM behaviour even in a linear geometry.[19] Recent theoretical studies indicate that the magnetic relaxation rate in lanthanide complexes strongly depends on the spin–phonon coupling,[40] and hence, restricting the flexibility of the molecule or offering a rigid environment may help remove low-lying vibrational modes,[41] which eventually helps to prevent fast magnetization reversal.

Considering the dominance of substituted Cp ligands[18,25] in isolating the top-performing Dy(III) based SIMs, it is worthwhile to investigate new possibilities and directions in organometallic chemistry. Besides adding bulky substituents to the Cp ligands or substituting them with heteroatoms, another possibility is to explore the spherical fullerenes and their substituted analogues to design Dy(III) based SMMs, as fullerenes are capable of trapping the metal ions inside the cage (endohedral metallofullerenes or EMFs)[42,43] and outside the cage (exohedral metallofullerenes).[44–48] In particular, significant progress has been made in endohedral metallofullerenes,[42,43,49–53] where encapsulation of lanthanides shows peculiar bonding and magnetic properties. Popov *et al.* have conducted pioneering work on the structure, stability, and cluster cage interactions in several cluster metallofullerenes of carbides, sulfides, and nitrides that exhibit peculiar single-ion magnetic characteristics.[49,50,54–57] Using computational tools, Rajaraman and coworkers have thoroughly investigated the role of the fullerene environment on the magnetic properties of Co(II) and Ln(III) based endohedral metallofullerenes.[58–60] In addition to lanthanides, there have been a handful of reports where the actinides have been encapsulated inside $C_{80}/C_{82}/C_{84}$ cages and thoroughly investigated to probe the electronic structure and bonding.[51–53] In contrast, the chemistry of exohedral metallofullerenes is somewhat limited as stabilizing highly symmetric sandwich complexes are very rare due to spherically delocalized distribution of 60-π electrons across 90 C–C bonds, leading to a considerable reduction in the π-electron density per C–C bond compared to localized C–C double bonds.[61,62] However, a few successful attempts have been made to disrupt the 60-π electron conjugation by saturating five α positions around a 5-membered ring of C_{60}, creating a fence around the $(Cp)^-$ ring of fullerene to yield $(C_{55}(CCH_3)_5)^-$, which can mimic the (Cp) ligands.[44] In this context, Nakamura and co-workers have reported a series of air-stable exohedral metallofullerene complexes with the general formula $[TM(C_{60}Me_5)Cp]$ (where TM = Fe(II), Ru(II) and Cp = cyclopentadienyl anion) which mimics ferrocene and its analogues.[44,63,64] Numerous theoretical reports suggest that all these transition metal-based exohedral fullerene complexes are highly stable in nature; however, the strength of the metal–ligand interactions is relatively weak compared to that of the ferrocene analogue.[47,65] Nakajima and coworkers have characterized the Ln_n–C_{60} multinuclear clusters using photoelectron spectroscopy, which shows that the Eu(II) and Ho(III) ions sit at the exohedral position in the cluster.[66,67] Since the structural and bonding motifs of the substituted fullerenes $(C_{55}(CCH_3)_5)^-$ closely resemble those of the $(Cp)^-$ ligands (see Fig. 1), the bulky $(C_{55}(CCH_3)_5)^-$ ligands have more potential to offer higher axiality while developing Dy(III) based organometallic sandwiched SIMs. In one of the seminal works, Rajaraman and co-workers have explored structural and magnetic properties in Dy(III) based corannulene complexes in the endo- and exohedral fashion.[68] Despite having ample experimental evidence of transition metal-based exohedral fullerenes,[44,63,69] to the best of our knowledge, there are no reports available in the literature that describe the complexation, geometry, electronic structure, and single-ion behaviour in lanthanide-based exohedral fullerene complexes.

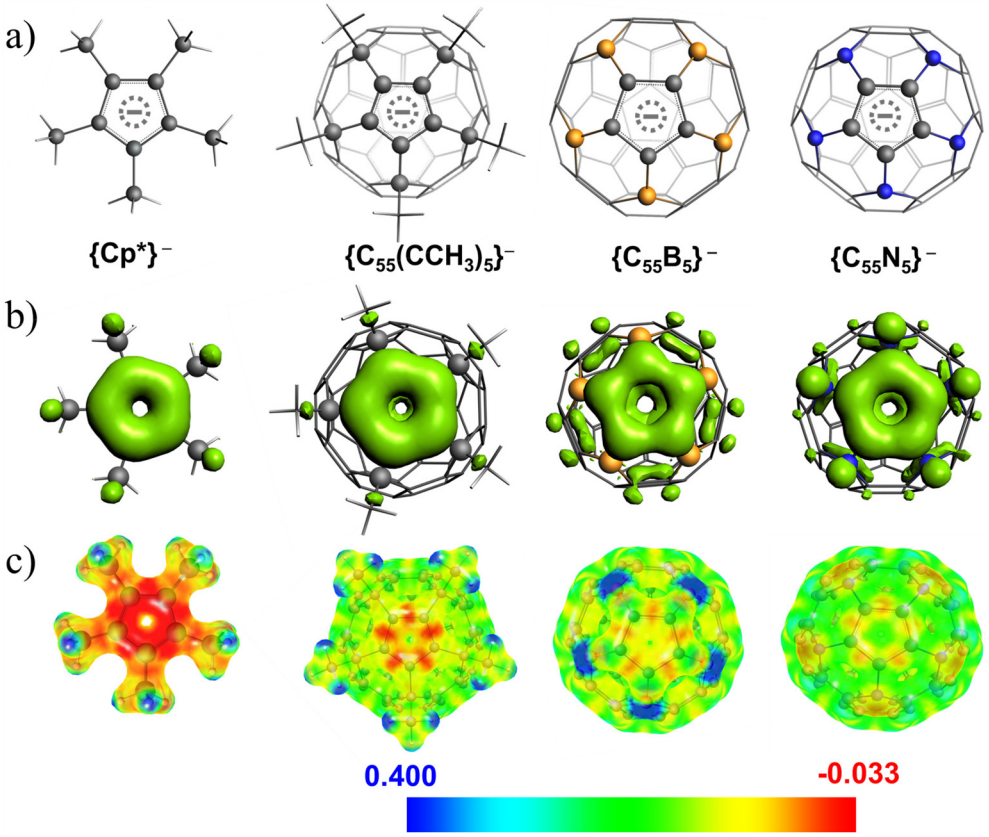

Fig. 1 (a) DFT optimized structures of Cp* and $(C_{55}X_5)^-$ (where X = CCH_3, B, and N) rings; (b) sum of orbital densities of the highest occupied molecular orbital (HOMO) and HOMO–1 of the Cp* and $(C_{55}X_5)^-$ rings plotted with an isosurface = 0.002 a.u.; and (c) molecular electrostatic potential maps (MEPs) of Cp* and $(C_{55}X_5)^-$ ligands. Color code: N (blue), B (orange), C (grey), and H (white).

Computational tools are indispensable in predicting the geometry, electronic structure, and magnetic properties of mononuclear and polynuclear open-shell metal complexes.[29] Both the scalar relativistic density functional theory (SR-DFT) and multireference-based complete active space self-consistent (CASSCF) methods are the main workhorses to study the electronic structure and single-ion magnetic behaviour in the mononuclear transition metal and lanthanide complexes. Particularly in molecular magnetism, computational tools play a profound role in predicting SIM performance, magnetic relaxation, and spin–phonon coupling.[29,41,70–73] Considering the potential of substituted fullerenes as η^5-donor ligands that can mimic the $(Cp)^-$ ligands,[44,63] we aim to explore the capabilities of three $(\eta^5\text{-}C_{55}X_5)^-$ ligands (where X = CCH_3, N or B) in stabilizing Dy(III) based SIMs as an alternative to the $[DyCp_2]^+$ family of complexes. Except for $(\eta^5\text{-}C_{55}(CCH_3)_5)^-$ ligands,[44,64] the $(\eta^5\text{-}C_{55}B_5)^-$/$(\eta^5\text{-}C_{55}N_5)^-$ ligands produced by exchanging five α-carbon atoms of fullerenes are purely hypothetical and have been investigated to assess the role of orbital interactions offered by B/N atoms compared to the CCH_3 group in stabilizing exohedral Dy(III) complexes.[74] In the present manuscript, we have studied eight exohedral metallofullerene complexes of the Dy(III) ion with the general formula $[Dy(\eta^5\text{-}C_{55}X_5)(C_mH_m)]$ (m = 4, 5, 6, 8 and X = CCH_3) and $[Dy(\eta^5\text{-}C_{55}X_5)_2]^+$ (where X = CCH_3, N or B) (see Scheme 1). Using SR-DFT calculations, we shed light on the thermodynamic stability and the nature of interaction energy in all the complexes. Bonding analysis was carried out using energy decomposition analysis (EDA) with a natural orbital for the chemical valence (EDA-NOCV)[75] approach and quantum theory of atoms in molecules (QTAIM) analysis.[76] Next, we performed CASSCF calculations on all the complexes to compute the single-ion anisotropy and relevant spin Hamiltonian (SH) parameters to analyze the SIM behaviour. Finally, we performed the magnetic relaxation analysis to shed light on the nature of QTM and Orbach relaxations.

Computational methodology

Geometry optimizations were carried out in the ORCA 5.0.3 code.[77,78] Geometry optimization was carried out using SR-DFT calculations at the BP86[29] level of theory. Scalar relativity was accounted for using the Douglas–Kroll–Hess (DKH) approximation as implemented in the ORCA code.[79] Here, we employed segmented all-electron relativistic contracted (SARC) triple zeta basis set SARC-DKH-TZVP[80] for the Dy atom and

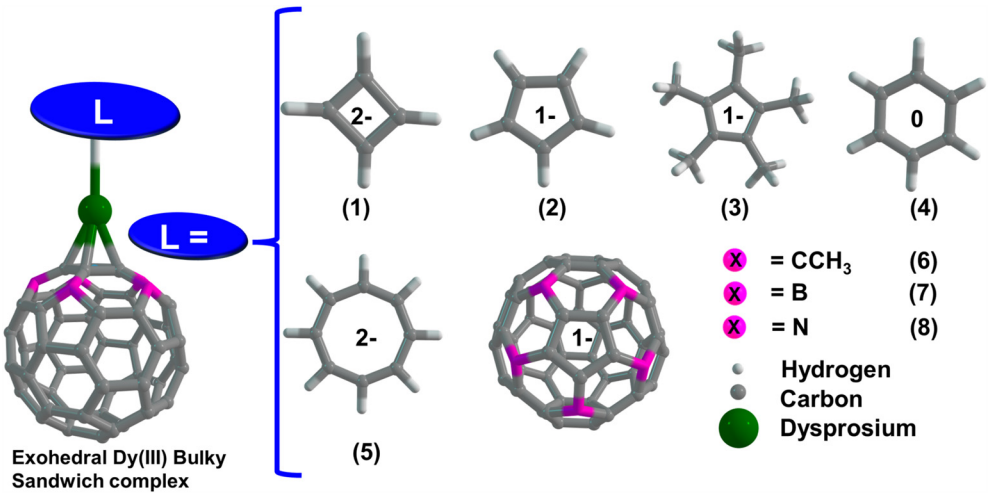

Scheme 1 Schematic representation of complexes **1–8**, with different ligands at axial positions. Color code: Dy (green), N (blue), B (pink), C (grey), and H (white).

DKH-adapted version of def2-SVP basis sets[81] for all other atoms. The dispersion interaction is addressed using Grimme's dispersion correction with the Becke–Johnson (D3BJ) scheme[82,83] as implemented in the ORCA. Vibrational frequency calculations on the DFT-optimized structures of complexes **1–8** show no negative frequency, which validates the stationary points as the local minimum. A tight SCF convergence criterion (1×10^{-8} E_h) was used for energy minimization. We used "*slowconv*" criteria and large integration grid settings (GRID9 for Dy) to achieve smooth energy convergence. Our geometry optimization methodology is highly effective in predicting the structure of open-shell mononuclear transition metal lanthanides and actinide complexes.[22,29,84] The reaction energetics are presented as formation energy (ΔE), enthalpy (ΔH), and free energy (ΔG), incorporating electronic energies along with corrections for zero-point vibrational energy. Eqn (1)–(3) have been employed to calculate ΔE, ΔH, and ΔG at 298.15K.

$$\Delta E = E_{\text{complex}} - E_{\text{Dy(III)}} - E_{(C_{55}X_5)} - E_{(C_mH_m)} \quad (1)$$

$$\Delta H = H_{\text{complex}} - H_{\text{Dy(III)}} - H_{(C_{55}X_5)} - H_{(C_mH_m)} \quad (2)$$

$$\Delta G = G_{\text{complex}} - G_{\text{Dy(III)}} - G_{(C_{55}X_5)} - G_{(C_mH_m)} \quad (3)$$

here, ΔE, ΔH, and ΔG are the electronic, enthalpy, and Gibbs free energy of complexation, respectively. E_{complex} is the electronic energy of the overall complex, $E_{(C_{55}X_5)}$ is the electronic energy of substituted fullerene $(C_{55}X_5)^-$ (X = CCH_3, B and N), $E_{(C_mH_m)}$ (where m = 4, 5 6, 8) is the electronic energy of the ring and $E_{\text{Dy(III)}}$ is the electronic energy of the free Dy(III) ion, for complexes **1–8**. Single-point energy calculations were performed on the DFT-optimized complexes **1–8** using the PBE0 functional[85] in the ADF 2021 code.[86] Here, we used Slater-type all-electron TZP basis sets[87,88] for Dy and DZP for other atoms. Scalar relativistic effects were treated using the zeroth-order regular approximation (ZORA)[89] without any frozen core approximation. Dispersion corrections were applied using Grimme's D3 corrections with Becke–Johnson damping (D3BJ).[82] To understand the nature of bonding, QTAIM analysis was performed on the DFT-optimized complexes **1–8** using ADF 2021 at the same level. We conducted EDA and its extended transition state theory, incorporating natural orbitals for chemical valence (ETS-NOCV) analysis, to gain insight into the bonding interactions between the fragments. Here, we computed the interaction energy by fragmenting complexes **1–8** into two fragments, $((C_mH_m)^{2-/1-/0}$ (m = 4, 5, 6, 8) and $(C_{55}X_5)^-$ (where X = CCH_3, N or B)) as fragment **1** and Dy(III) as fragment **2** using the ADF software. The total interaction energy ΔE_{int} is broken down into four components within the ETS energy breakdown scheme[75] as shown in eqn (4);

$$\Delta E_{\text{int}} = \Delta E_{\text{elstat}} + \Delta E_{\text{Pauli}} + \Delta E_{\text{orb}} + \Delta E_{\text{disp}} \quad (4)$$

ΔE_{elstat} signifies the traditional electrostatic interaction between fragment densities in the promolecule directly tied to the ionic bonding between those fragments. ΔE_{Pauli} factors in Pauli repulsion indicate the energy increase resulting from applying the Pauli exclusion principle to promolecular densities, which are inherently repulsive. ΔE_{disp} includes the contribution from the DFT-D3 dispersion correction,[82] which is always stabilizing in nature. ΔE_{orb} represents the energy associated with orbital interaction, reflecting the reduction in energy as promolecular densities mix and relax, linked to the covalent bonding between metal and ligands. The orbital interaction energy, ΔE_{orb} involves the relaxation of Ψ^0 to converged wave function Ψ with respect to ρ. The orbital interaction energy ΔE_{orb} can be split into pairwise contributions from the interacting orbitals of the fragments by applying the NOCV technique to EDA. The total complementary orbital pairs (Ψ_{-k}, Ψ_k) with equal and opposite eigenvalues

represent the corresponding deformation density ($\Delta\rho^{orb}$), whereas noninteracting orbitals have zero eigenvalues, as shown in eqn (5).

$$\Delta\rho^{orb}(r) = \rho - \rho^0 = \sum_{k=1}^{\frac{N}{2}} \nu_k[-\Psi_{-k}{}^2(r) + \Psi_k{}^2(r)] + \sum_{k=1}^{\frac{N}{2}} \Delta\rho_k(r) \quad (5)$$

This includes charge transfer, electron pair bonding, and polarization. This systematic breakdown of physical components provides informative and effective insight into bonding, particularly in systems with clear σ/π separation.

Electronic and magnetic properties for complexes **1–8** were carried out using the complete-active space self-consistent field (CASSCF) method[90] in the ORCA code. Here, we have used an active space of CAS(9,7), *i.e.* nine active electrons (f^9 configurations) in seven active 4f orbitals and computed all the 21 sextet states emerging from the ^6H, ^6F, and ^6P configurations. These 21 sextets states are good enough for the $^6H_{15/2}$ SOC spectrum and the magnetic properties of Dy(III) based SIMs.[91–96] Spin–orbit calculations were carried out using 21 sextet states with spin–orbit mean field (SOMF-IX) operator and second-order Douglas–Kroll–Hess (DKH2) method[79] with a "*picturechange 2*" option as implemented in ORCA. In addition, we have performed CASSCF calculations, including all 21 sextets, 224 quartets, and 490 doublet roots, and calculations suggest that only 21 sextet roots are sufficient to compute the energy span of eight low-lying KDs in Dy(III) complexes (see Table S18† for details). Next, we utilized a standalone SINGLE_ANISO module[97] for the *g*-values, wavefunction decompositions, crystal field parameters, and transition magnetic moments between the KDs. In addition to *ab initio* constructed magnetic relaxation based on the average value of transition magnetic moments, we have also computed the effective demagnetization barriers proposed by Aravena *et al.*[70] to analyze the Orbach relaxation process and to predict the blocking temperature.[98] This method utilizes the energy of the eight Kramers doublets and the magnetic transition dipole moment related to the transition between the respective KDs (*i.e.*, $+1 \rightarrow -1$) from the CAS(9,7) calculations. This method involves the use of eqn (6),

$$U_{eff}(T) = \sum_{i=1}^{M} \frac{k_i(T)}{N_k} E_i \quad (6)$$

Here, M denotes the number of KDs, k_i denotes the demagnetization rates of the KDs of energies E_i, and N_k is a normalization factor for k_i as shown in eqn (7):

$$k_i(T) = \frac{\exp\left(-\frac{\varepsilon}{k_B T}\right)}{Z} k_{QT,i} \quad (7)$$

k_B is the Boltzmann constant, $k_{QT,i}$ represents the magnetic transition dipole moment and T and Z are the temperature and the partition function, respectively. In another work by Aravena, they proposed an approximate method to determine the blocking temperature (T_B) for the Orbach relaxation by dividing the energy barrier computed by 28, which matched the experimental values quite well. Hence, we have also used this method to predict the blocking temperature for the complexes under study.

Results and discussion

Here, we have examined eight exohedral metallofullerene complexes named $[Dy(\eta^5\text{-}C_{55}X_5)(\eta^4\text{-}C_4H_4)]$ (**1**), $[Dy(\eta^5\text{-}C_{55}X_5)(\eta^5\text{-}Cp)]^+$ (**2**), $[Dy(\eta^5\text{-}C_{55}X_5)(\eta^5\text{-}Cp^*)]^+$ (**3**) $[Dy(\eta^5\text{-}C_{55}X_5)(\eta^6\text{-}C_6H_6)]^{2+}$ (**4**), $[Dy(\eta^5\text{-}C_{55}X_5)(\eta^8\text{-}C_8H_8)]$ (**5**), $[Dy(\eta^5\text{-}C_{55}X_5)_2]^+$ (**6**) $[Dy(\eta^5\text{-}C_{55}B_5)_2]^+$ (**7**) and $[Dy(\eta^5\text{-}C_{55}N_5)_2]^+$ (**8**) (where X = CCH_3) for our study. DFT optimization of complexes **1–8** was carried out in the gas phase without symmetry constraints (see the Computational methodology section for details). DFT-optimized coordinates are provided in the ESI.† In complexes **1–5**, the computed average Dy–L_{cent} (L_{cent} = bond distance between Dy and centroid of the C_mH_m ring) bond distances decrease as the ring size increases (see Table S1†). In complexes **1–4**, we have observed a stabilization of the bent geometry with $\angle L_{cent}$–Dy–L_{cent} of approximately ~157°, 145°, 161°, and 153°, respectively. The presence of the Cp* ligand in **3** offers higher steric repulsion than in **2** (Cp ligands), resulting in a large $\angle L_{cent}$–Dy–L_{cent} bond angle for **3**. Moreover, we compared the structural parameters of complexes **2** and **3** with the DFT optimized geometry of non-bucky analogues $[DyCp_2]^+$ (**2a**) and $[DyCp^*_2]^+$ (**3a**) complexes, which suggests that the bulkiness of substituted $(C_{55}X_5)^-$ cages (X = CCH_3) naturally offers more linearity in the $\angle L_{cent}$–Dy–L_{cent} bond angle, which is the key for maximizing the axiality in the Dy(III) based sandwiched complexes (see Table S1†). The DFT optimized geometry of complex **5** nicely matches the previously reported X-ray crystal structure of the [Cp*DyCOT] complex,[99] highlighting the goodness of our computational methodology in reproducing heteroleptic organometallic sandwiched complexes. In complexes **6–8**, we observed that the avg. Dy–L_{cent} $(C_{55}X_5)^-$ bond distance is 2.351, 2.284, and 2.389 Å, respectively, and the $\angle L_{cent}$–Dy–L_{cent} bond angle is close to 180°, highlighting the importance of the steric effect caused by the $(C_{55}X_5)^-$ ring which forces a linear geometry around the Dy(III) ion. Structural analysis of all the complexes reveals that the average Dy–L_{cent} $(C_{55}X_5)^-$ bond distances calculated from the centroid of the ring range between 2.284 and 2.389 Å, which is slightly larger than the average Dy–Cp/Dy–Cp* bond distance in complexes **2–3**, indicating a comparatively weaker bonding in complexes **6–8**. DFT optimization predicts the stabilization of staggered D_{5d} local symmetry around the Dy(III) ion in complexes **6–8**. The detailed structural parameters for all the complexes are provided in Table S1.† In addition, we optimized the geometry of Cp* and $(C_{55}X_5)^-$ ligands, and we observed that the highest occupied molecular orbitals (HOMOs) are mainly the π-electron clouds on the five-membered ring of the ligands. It is evident from the observed HOMOs of $(C_{55}X_5)^-$ rings (where X = B/N) that the π-conjugation in fullerenes is not completely broken when α-C

atoms are replaced by B/N atoms. In contrast, for the $(C_{55}(CCH_3)_5)^-$ ring, the sum of orbital densities of HOMO and HOMO−1 nicely resembles the Cp* ligands as the sp^3 hybridized α-C carbon completely breaks the π-conjugation in the $(C_{55}(CCH_3)_5)^-$ ring, making them electron-rich donors compared to B/N analogues (see Fig. 1). The computed molecular electrostatic potential of $(C_{55}X_5)^-$ ligands reveals that the five-membered rings are relatively electron deficient in nature compared to the Cp* ligands, which has direct consequences on metal–ligand interactions.

Interaction energy and thermodynamics

To compute the interaction energies (IE) among the fragments in metallocenes, we designated the metal cation Dy(III) as a Y fragment, while the C_mH_m ring and $(C_{55}X_5)^-$ were identified as X and X′ fragments, respectively. The interaction energy was determined using eqn (8):

$$IE_{total} = E^{XYX'}_{free} - (E^{X}_{frozen} + E^{Y}_{frozen} + E^{X'}_{frozen}) \quad (8)$$

Here $E^{XYX'}_{free}$, is the energy of the optimized geometry of the XYX′ complex (**1–8**), whereas E^{X}_{frozen} + E^{Y}_{frozen} + $E^{X'}_{frozen}$ are the energies of X, Y, and X′ frozen components in the optimized geometry of the XYX′ complex, respectively.

Table 1 shows that the interaction between the Dy(III) center and the two ligands ((C_mH_m) and $(C_{55}X_5)^-$) is favorable, showing sizable interaction energy values ranging between ∼700 and 1200 kcal mol^{-1}. Since the energy of the Dy(III) ion and $(C_{55}X_5)^-$ remains constant throughout the series in complexes **1–5**, the key factor devising overall interaction energy is the E_X and the $E_{XYX'}$ component, which is the energy of the (C_mH_m) fragment and the total energy of the complexes respectively. The highest interaction (IE_{Total}) is observed for complexes **1** and **5**, which feature dianionic $(C_4H_4)^{2-}$ and $(C_8H_8)^{2-}$ rings, while the lowest interaction is observed for complex **4**, possessing neutral (C_6H_6) as the X fragment. An intermediate value of IE_{Total} is observed for complexes **2**, **3**, **6**, **7**, and **8**, which possess monoanionic (C_mH_m) rings. The observed trend indicates that the IE_{Total} value strongly depends on the strength of the electrostatic interaction between fragments (*vide infra*). A nearly identical value of IE_{Total} is obtained for complexes **2** and **3**, which suggests that the Cp and Cp* rings interact almost similarly with the other components. Among complexes **6–8**, where both the X and X′ components are substituted fullerenes $(C_{55}X_5)^-$, we observed the following trend in the IE_{Total} value **6** > **7** ≈ **8**, with the IE_{Total} in **6** nearly ∼50 kcal mol^{-1} higher than **7** and **8**. In addition, we have computed thermodynamic parameters at 298.15 K to predict the formation energy of these complexes, and the computed change in the free energies is highly exothermic for all the complexes, which is in line with IE_{Total} analysis (see Tables S3 and S4†).

Next, we performed EDA analysis by fragmenting complexes **1–8** into two fragments, Dy(III) as fragment 1 carrying a tri positive charge, whereas the other two rings $((C_mH_m)^{2-/1-/0}$ and $(C_{55}X_5)^-)$ as fragment 2.[100] This fragmentation scheme allowed us to understand the nature and strength of the binding interaction between the corresponding fragments. EDA analysis predicts a negative value of the total interaction energy (ΔE_{int}) for all the complexes, which aligns with interaction energy analysis and thermodynamic calculation (see Table 2). EDA calculations predict the following trend in the ΔE_{int} value: **5** > **1** > **3** ≈ 2 > **6** > **7** > **8** > **4**, with the most considerable ΔE_{int} value observed for **5** while the smallest ΔE_{int} value is reported for **4**. The decomposition of the interaction energy suggests that both the orbital interactions (ΔE_{orb}) and the electrostatic interaction (ΔE_{elstat}) are the most significant contributors to the total interaction energy (ΔE_{int}), with the former one being relatively more dominant compared to the ΔE_{elstat} values. We observed the following trend in the ΔE_{elstat} value: **5** > **1** > 2 ≈ **3** > **6** > **7** > **8** > **4**, which agrees with the trend observed for the ΔE_{int} value, indicating that the ΔE_{elstat} components control the overall interaction energy in complexes **1–8**.

The orbital interaction is the most vital contributor to the overall interaction energy with the following trend in ΔE_{orb} values: **5** > **1** > **7** > **3** > **8** > **2** ≈ **6** > **4**. The most substantial orbital interaction is observed in complexes **1** (∼701 kcal mol^{-1}) and **5** (∼762 kcal mol^{-1}) due to the strong interaction between the Dy(III) orbitals (4f and 5d) with the π-cloud of the $(C_4H_4)^{2-}$ and $(C_8H_8)^{2-}$ ligands. Due to similar ligand scaffolds in complexes **2** and **3**, we observed nearly similar ΔE_{orb} values for these complexes. The weakest ΔE_{orb} value of ∼609 kcal mol^{-1} is observed for complex **4**. It is important to note here that, unlike trends observed in ΔE_{elstat} values, the variation in the ΔE_{orb} value is close to 20% within the studied complexes, which manifests the weak lanthanide-ligand covalency.

Table 1 DFT computed electronic energies of fragments and complexes, and the total interaction energies for complexes **1–8**

Complex	**1**	**2**	**3**	**4**	**5**	**6**	**7**	**8**
$E_X(E_h)$	−154.4	−193.5	−390.0	−232.2	−309.4	−2485.6	−2219.8	−2369.3
$E_Y(E_h)$	−12 148.3	−12 148.3	−12 148.3	−12 148.3	−12 148.3	−12 148.3	−12 148.3	−12 148.3
$E_{X'}(E_h)$	−2485.6	−2485.6	−2485.6	−2485.6	−2485.6	−2485.6	−2219.8	−2369.3
$E_{XYX'}(E_h)$	−14 790.2	−14 828.9	−15 025.5	−14 867.2	−14 945.2	−17 121.0	−16 589.2	−16 888.2
$IE_{Total}(E_h)$	−1.9	−1.5	−1.5	−1.1	−1.9	−1.4	−1.3	−1.3
IE_{Total}(kcal mol^{-1})	−1211.2	−923.1	−933.1	−690.2	−1177.7	−895.1	−834.9	−823.6

Table 2 PBE0-D3(BJ)/TZP computed EDA analysis of complexes **1–8**. All the energy values provided here are in kcal mol^{-1}

Energy	1	2	3	4	5	6	7	8
ΔE_{Pauli}	192.1	208.7	225.2	207.6	253.8	186.0	183.5	158.5
ΔE_{elstat}	−709.0	−610.0	−604.9	−353.0	−755.6	−512.4	−440.3	−408.8
ΔE_{orb}	−700.8	−623.3	−653.9	−608.5	−761.5	−623.5	−656.6	−639.9
ΔE_{disp}	−7.4	−7.1	19.0	−7.1	−7.2	−10.8	−4.9	−6.9
ΔE_{int}	−1225.0	−1031.7	−1042.6	−761.0	−1270.5	−960.7	−918.4	−897.0
$\Delta E_{\text{orb(1)}}$	−282.6	−262.2	−269.1	−311.4	−227.4	−232.8	−249.9	−238.4
$\Delta E_{\text{orb(2)}}$	−216.5	−237.9	−231.2	−265.4	−206.2	−233.4	−249.8	−292.6
Total	−499.1	−500.1	−500.3	−576.8	−433.6	−466.2	−499.8	−531.0
% ΔE_{orb}	71.2	80.2	76.5	94.8	56.9	74.8	76.1	83.0

$\Delta E_{\text{int}} = \Delta E_{\text{elstat}} + \Delta E_{\text{Pauli}} + \Delta E_{\text{orb}} + \Delta E_{\text{disp}}$

To further decompose the origin of orbital interactions, we have performed an ETS-NOCV[75,100,101] analysis on complexes **1–8**. In the ETS-NOCV technique, orbital interaction energy (ΔE_{orb}) is broken down into contributions from each NOCV (donor–acceptor) pair, which can be linked to specific bonding types between fragments, such as σ and π bonding. Each interaction $\Delta E_{\text{orb}(i)}$ is assigned a numerical energy value through visual inspection of NOCVs. NOCVs can be used to visually explore ΔE_{orb}, represented by the eigenfunctions (Ψ_i) of the density difference between molecular and promolecular densities. Each pair of NOCVs corresponds to two orbitals with equal and opposite eigenvalues(ν_i). As a molecule forms from a promolecule, electron density transfers through channels described by these NOCV pairs. The magnitude of NOCV eigenvalues indicates the importance of each pair in bond formation. The first four deformation densities ($\Delta\rho_i$) corresponding to the NOCV pairs for complexes **1–8** are depicted in Table S7,† starting with the pair with the greatest eigenvalue. Red areas of $\Delta\rho_i$ show charge depletion, whereas blue areas indicate charge accumulation upon bond formation. From deformation densities, it is evident that the red region is mainly located on the coordinating ligands while the blue region is located on the Dy(III) ion, suggesting an electron flow from the ligand to metal orbitals. Based on the visual inspection of the NOCVs, the $\Delta E_{\text{orb(1)}}$ and $\Delta E_{\text{orb(2)}}$ have the highest magnitude in complexes **1–8**, which contribute around ∼70–80% of the total ΔE_{orb} value (see Table 2). A closer inspection of NOCV pairs corresponding to $\Delta E_{\text{orb(1)}}$ and $\Delta E_{\text{orb(2)}}$ suggests that the giant orbital interaction energy arises due to π-type interaction, where electron flow occurs predominantly from the $2p_x$ orbital of the coordinating ligand (π-cloud) to the 4f orbital of the Dy(III) ion. This indicates the presence of sizable 4f-ligand covalency in all the studied complexes. On the other hand, the $\Delta E_{\text{orb(3)}}$ and $\Delta E_{\text{orb(4)}}$ correspond to the electron flow from the $2p_x$ orbitals of the coordinating ligand (π-cloud) to the $5d_{yz}/5d_{xz}$ orbital of the Dy(III) ion and roughly contribute ∼10–30% of the total ΔE_{orb} value. Due to the difference in X and X′ ligands in complexes **1–5**, we observed different $\Delta E_{\text{orb(1)}}$ and $\Delta E_{\text{orb(2)}}$ values, while complexes **6–8** show nearly similar values. In complex **6**, the $\Delta E_{\text{orb(1)}}$ and $\Delta E_{\text{orb(2)}}$ values are ∼−188 kcal mol^{-1} and −189 kcal mol^{-1}, which contribute around ∼74.8% of the total ΔE_{orb} value (see Fig. 2). The $\Delta E_{\text{orb(3)}}$ and $\Delta E_{\text{orb(4)}}$ values are ∼−41 and −40 kcal mol^{-1}, which corresponds to the electron flow from the $2p_x$ orbitals of the coordinating ligand (π-cloud) to the $5d_{yz}/5d_{xz}$ orbital of the Dy(III) ion, indicating 5d-covalency in the studied complexes(see Fig. 2). NPA analysis of the fragments also shows a prominent gain in the 5d orbitals (+0.30 a.u.) and 4f orbitals (+0.11 a.u.) upon complexation, confirming the participation of 4f and 5d orbitals in the bonding (see Table S8†).

EDA computed dispersion interactions are stabilizing in nature and contribute ∼1–2% of the total interaction energy. The highest dispersion interaction (ΔE_{disp}) is observed in complexes **3** (∼9 kcal mol^{-1}) and **6** (∼11 kcal mol^{-1}) due to the presence of the methyl group in the Cp* and the $(C_{55}(CCH_3)_5)^-$ ligands, resulting in sizable non-covalent interaction. To further probe this, we performed a non-covalent interaction (NCI) analysis,[102,103] which offers a way to present non-covalent interactions in real space. In complexes **1–5**, the presence of $-CH_3$ groups in $(C_{55}(CCH_3)_5)^-$ fragments results in sizeable van der Waals (vdW) interaction between the fragments, which is visible in the NCI plots. The most considerable dispersion interaction for **6** (10.8 kcal mol^{-1}) results from strong vdW interactions between the two bulky $(C_{55}(CCH_3)_5)^-$ ligands (see Fig. 3). Replacement of CH_3 groups with B/N atoms significantly reduces the non-covalent interactions in **7** and **8**, resulting in weaker ΔE_{int} values for these complexes compared to **6**.

Next, we performed the QTAIM analysis[76,106] for all the complexes to further quantify the nature of the bond between the Dy and ligands (see Table S9† and Fig. 4). QTAIM divides molecular electron density into separate regions using surfaces where $\nabla\rho(r)\cdot n(r) = 0$. Each region or basin, usually corresponds to an atom. Critical points such as bond critical points (BCPs) occur where bond paths intersect interatomic surfaces. BCPs are represented in red, and ring critical points (RCPs) in green. The values of $(-G/V)_{\text{BCP}} > 1$ at the critical points signify ionic or non-covalent bonding, where local kinetic energy prevails over potential energy. On the

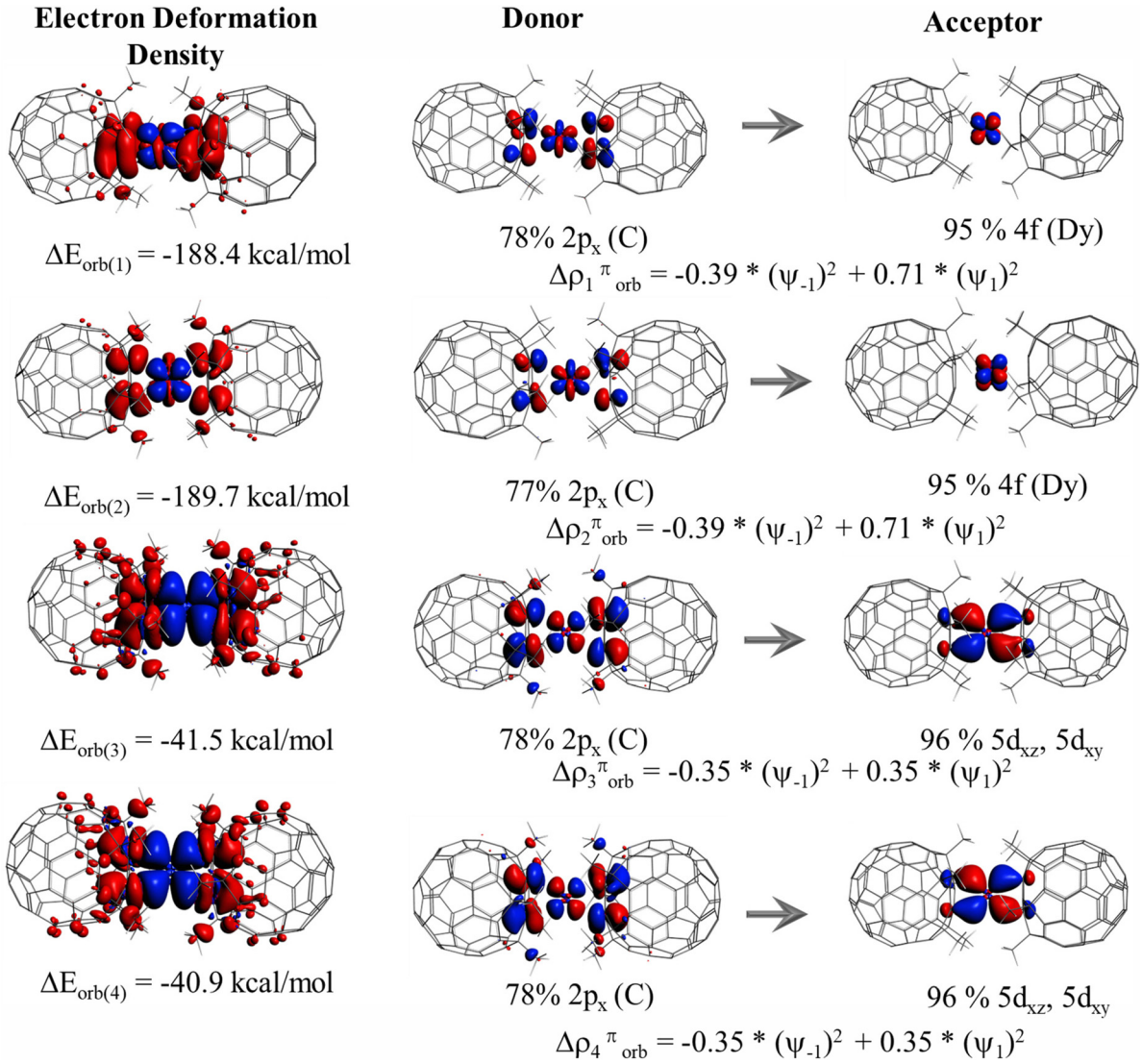

Fig. 2 ETS-NOCV computed electron deformation density (EDD) and corresponding donor and acceptor pair for complex **6** computed at the ZORA-PBE0-D3(BJ)/TZP level of theory. EDD is plotted with an isovalue of 0.0001 a.u, where the blue region shows charge depletion, whereas the red region shows charge accumulation.

other hand, values ranging from 0.5 to 1 indicate partial covalency.[107] Based on Table S9,† it is apparent that all eight complexes in our study have $|G/V|_{BCP}$ values below 1, indicating the presence of partial covalency. Typically, electron densities $\rho(r)$ exceeding 0.2 atomic units (a.u.) with $\nabla^2\rho(r) < 0$ are characteristic of covalent bonds, while those below 0.1 a.u. with $\nabla^2\rho(r) > 0$ suggest a more ionic bonding nature.[108] In all cases, we observe $\rho(r)$ less than 0.05 a.u (<0.1 a.u.) and $\nabla^2\rho(r) \sim 0.1(>0)$, suggestive of ionic bonding. To conclude, the Dy–C_{ligand} bonds in complexes **1–8** are predominantly ionic in nature since $\rho(r)$ is a more reliable parameter to quantify the nature of bonds.[109,110] The computed average electron density $\rho(r)$ suggests that the nature of bonding in hybrid bucky complexes (**1–5**) is nearly similar to di-bucky analogues (**6–8**), where the former ones are marginally more ionic in nature.

Magnetic anisotropy analysis in complexes 1–8

CASSCF calculations predict stabilization of m_J $|\pm15/2\rangle$ for all the complexes except for **5**, where the ligand field stabilizes m_J $|\pm9/2\rangle$ as the ground state (see Fig. 5). In complex **1**, the Dy(III) ion is sandwiched between the cyclobutadiene dianion $(C_4H_4)^{2-}$ ligand and the $(C_{55}(CCH_3)_5)^-$ ligand with a bent $\angle L_{cent}$–Dy–L_{cent} angle of 156.9° degree. CASSCF calculations predict the span of the eight low-lying KDs derived from the $^6H_{15/2}$ ground multiplet over an energy range of approximately 1649.2 cm^{-1}, with the first excited KD at approximately 487.4 cm^{-1} for complex **1**. The computed ground state *g*-values are highly axial in nature (g_{zz} = 19.980) with extremely weak transverse components ($g_{xx} = g_{yy} = 1 \times 10^{-4}$) (see Table S10†).

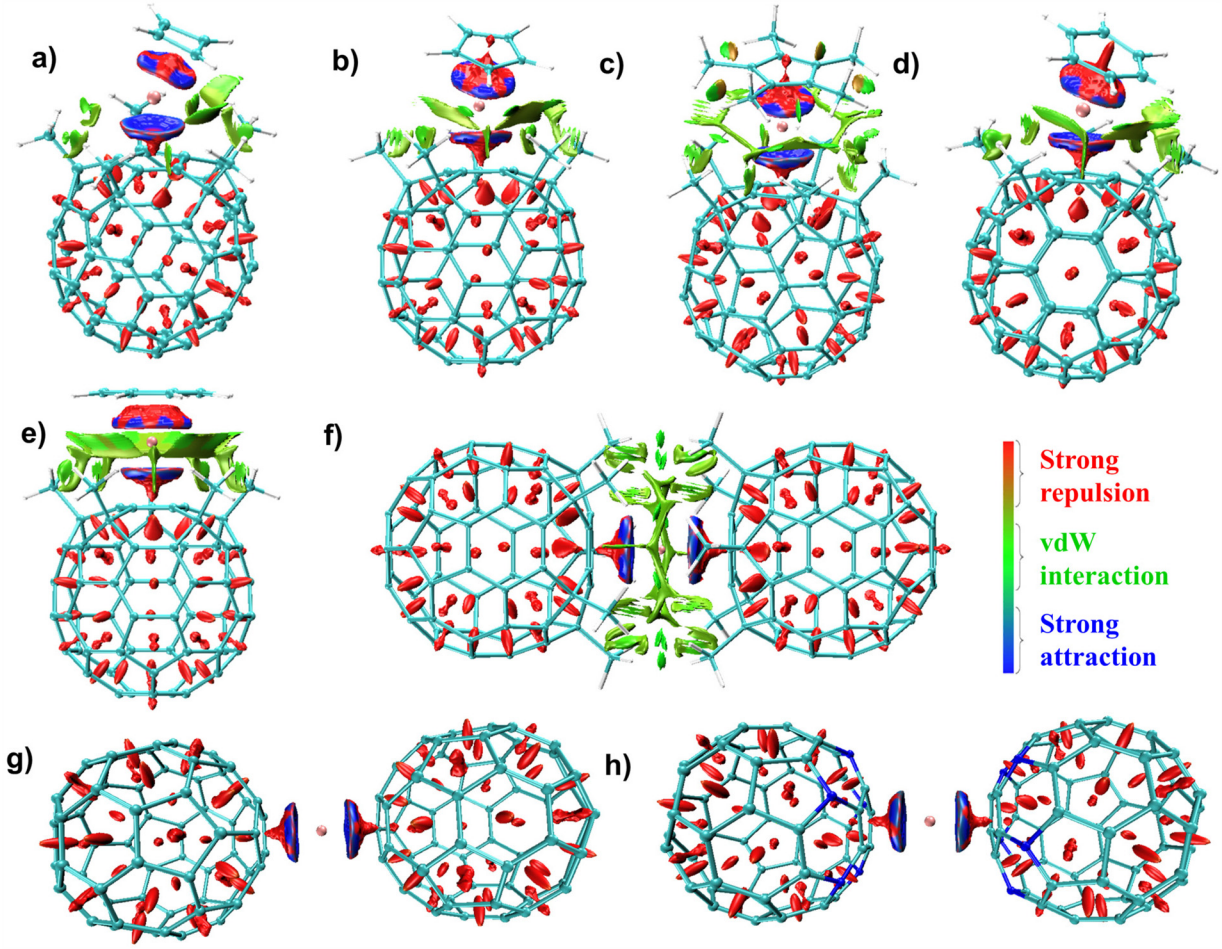

Fig. 3 (a)–(h) Non-covalent interaction (NCI) plots for complexes **1–8**. The isosurfaces are colour-coded based on the sign of the Laplacian (ρ) at a contour value of 0.05 a.u. Blue color denotes strong attraction (–ve ρ), green indicates vdW interactions ($\rho \sim 0$), and red indicates repulsive interaction (+ve ρ). Images were generated using Multiwfn[104] and VMD software.[105]

This is further explained by wavefunction decomposition analysis showing 99% m_J $|\pm 15/2\rangle$ as the ground state with no mixing from the other excited KDs (see Table S15†). The principal *z*-axis of the *g*-tensor passes through the centre of the $(C_4H_4)^{2-}$ ligand. Analysis of the *g*-tensor orientation of all eight KDs suggests that the g_{zz} orientation up to the 6th KD is nearly collinear (≤10 degrees), indicating that magnetization can be blocked up to this KD. The g_{zz} orientation of the 7th KD deviates by an angle of 94.3° from the ground state KD, indicating that magnetization reversal is likely to occur *via* this state. The CASSCF computed U_{cal} value is 1538.6 cm^{-1} (2154.0 K) for **1** (see Table 3). The computed transverse magnetic moment between the ground state KDs is negligible ($2.43 \times 10^{-7}\mu_B$), indicating complete quenching of QTM within the ground state KDs. Moreover, the computed transverse magnetic moment between the ground and excited KDs is always significantly higher than the values obtained within the KDs, highlighting that the thermally activated Orbach process is more dominant until the 7th KD as the QTM values are minimal. Due to the lack of linearity in the $\angle L_{cent}$–Dy–L_{cent} angle of **1**, we have not observed the complete blockade of magnetization up to the 7th KD.

Next, we analyzed the magnetic anisotropy in complexes **2** and **3** (see Tables S10 and S12†), which only differ with respect to Cp/Cp* ligands. As a result of the bulky effect of the Cp* ligand, we observed a relatively more linear $\angle L_{cent}$–Dy–L_{cent} angle in **3** (160.8°) compared to **2** (145.2°). The energies of eight low-lying KDs span over an energy range of 1423.5 and 1675.4 cm^{-1} for complexes **2** and **3**, respectively. The energy span of **2** is shrunk by ~15% compared to **3** due to the large bent angle, which decreases the axial ligand field strength. The computed *g*-values are highly axial in nature g_{zz} = 19.944 and $g_{xx} = g_{yy} = 1 \times 10^{-4}$ (g_{zz} = 19.986, $g_{xx} = g_{yy} = 1 \times 10^{-4}$) with a negligible transverse component in the *g*-values for **2**(**3**). The principal *z*-axis of the g-tensor passes through the centroid of the Cp/Cp* rings in **2** and **3**, respectively. The wavefunction decomposition analysis reveals stabilization of pure m_J $|\pm 15/2\rangle$ as the ground state for **2** and **3** (see Table S15†). Consequently, the computed transverse magnetic moment between the ground state KDs is extremely weak ($1.46 \times 10^{-6}\mu_B$ (**2**) and 6.55

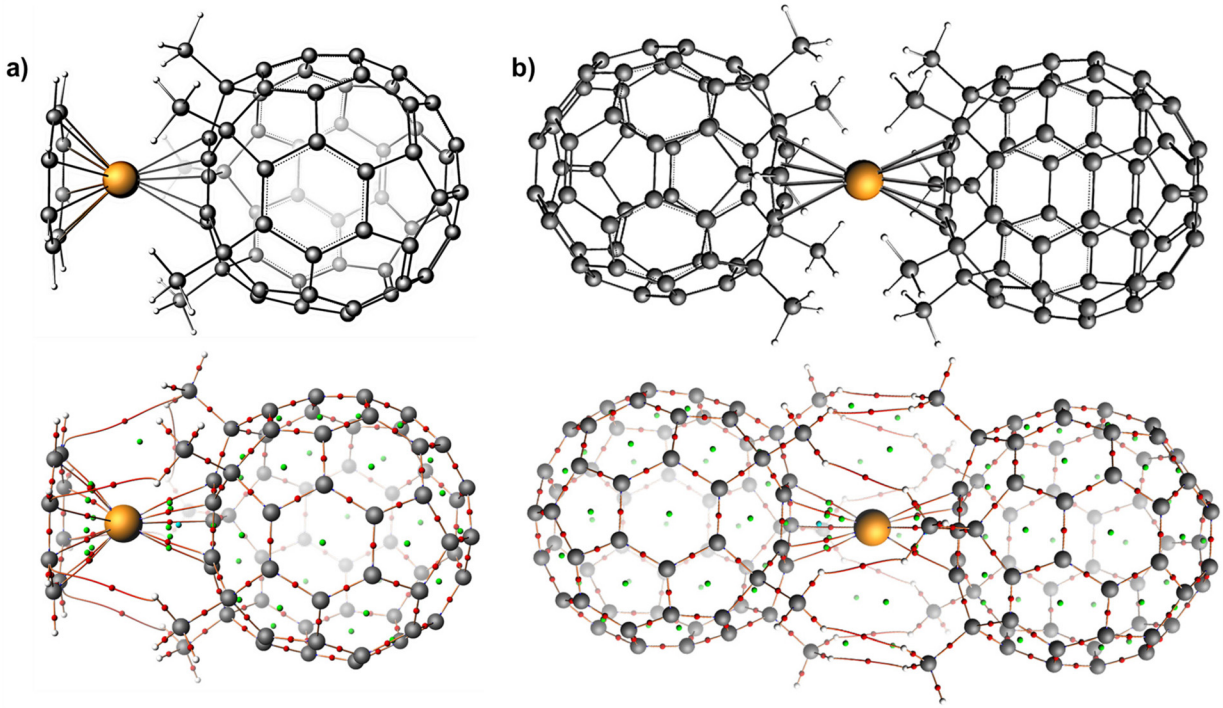

Fig. 4 PBE0-D3(BJ)/TZP computed QTAIM topology maps for (a) complex **5** (b) complex **6**. Colour code: Dy (orange), C (grey), H (white).

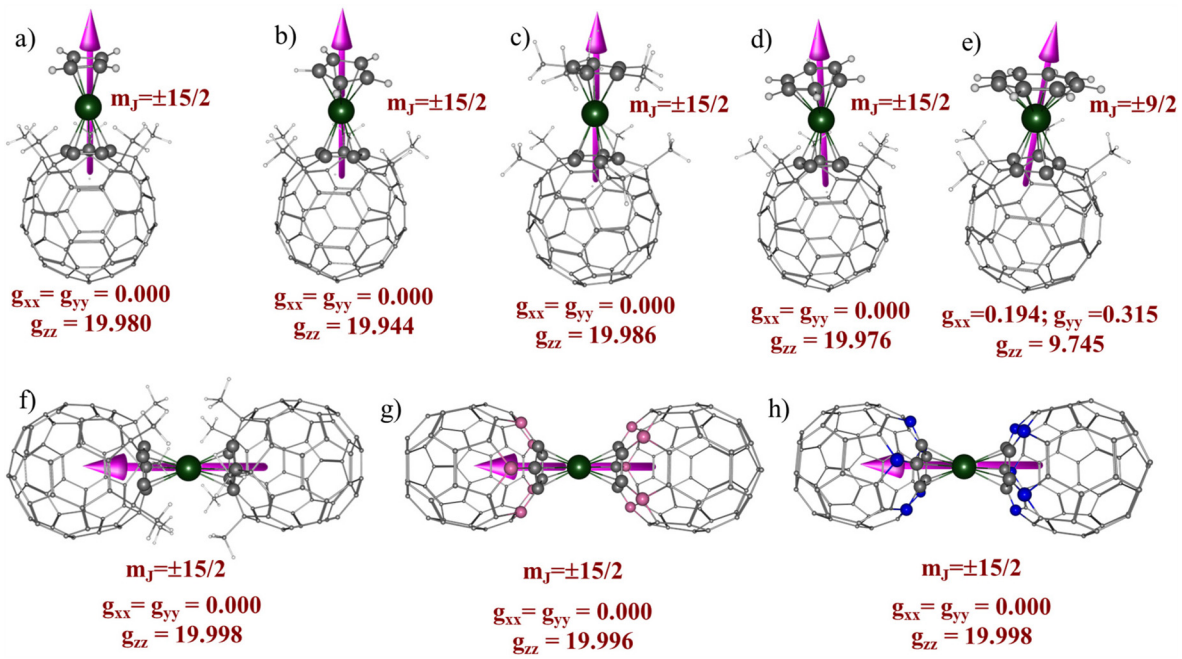

Fig. 5 (a)–(h) CASSCF computed ground state *g*-values, *g*-tensor orientation and corresponding wavefunction in complexes **1–8**, respectively. Colour code: Dy (green), N (blue), B (pink), C (grey), and H (white).

$\times 10^{-8}\mu_B$ (**3**)), which directly indicates that ground state QTM is quenched in both the complexes (see Table 3). For **3**, the transverse magnetic moment between the ground state KD is two orders smaller than **2**, indicating a stronger axial ligand field offered by the Cp* ligand helps to quench the ground state QTM. The *ab initio* computed blockade barrier suggests magnetization blockade up to the 6th KD, and magnetization relaxation is likely to occur *via* the 7th KD, which is mainly m_J $|\pm 3/2\rangle$

Table 3 SINGLE_ANISO computed energies of the ground and first excited Kramers doublets (KD), accompanied by their respective g-values, differences in g_{zz} orientation axes (θ), tunnelling coefficients (k_{QTM}), blocking barrier (U_{cal}), effective demagnetization barrier (U_{eff}) and blocking temperature (T_B)

	KD	g_{xx}	g_{yy}	g_{zz}	θ (°)	k_{QTM}	U_{cal} (cm^{-1})	U_{eff} (cm^{-1})	T_B (K)
1	KD1	0.000	0.000	19.980	—	2.43×10^{-7}	1538.6	1501.0	53.6
	KD7	3.227	4.480	7.803	94.3	2.04×10			
2	KD1	0.000	0.000	19.944	—	1.46×10^{-6}	1305.0	1338.0	47.7
	KD7	8.519	8.157	2.690	0.6	2.78×10			
2a	KD1	0.000	0.000	19.890	—	4.53×10^{-6}	1111.2	1181.0	42.2
	KD6	4.089	4.876	11.240	90.9	2.69×10			
3	KD1	0.000	0.000	19.986	—	6.55×10^{-8}	1569.5	1627.5	58.1
	KD7	2.742	3.097	3.619	10.4	9.77×10^{-1}			
3a	KD1	0.000	0.000	19.970	—	6.02×10^{-7}	1551.5	1589	56.8
	KD7	7.945	6.819	3.024	0.5	2.46×10			
4	KD1	0.000	0.000	19.976	—	1.71×10^{-7}	1124.8	1133.0	40.5
	KD7	3.309	3.384	7.521	82.4	1.87×10			
5	KD1	0.194	0.315	9.745	—	8.48×10^{-2}	108.4	95.2	3.4
	KD6	4.750	6.936	9.358	99.2	2.63×10			
6	KD1	0.000	0.000	19.998	—	3.99×10^{-9}	1573.7	1533.0	54.8
	KD8	11.607	9.451	1.188	0.5	3.51×10			
7	KD1	0.000	0.000	19.996	—	2.37×10^{-7}	1284.1	1235.0	44.1
	KD8	11.322	9.789	1.212	0.4	3.52×10			
8	KD1	0.000	0.000	19.998	—	8.99×10^{-8}	1347.0	1314.0	46.9
	KD8	11.189	9.907	1.201	0.4	3.51×10			

in nature. The computed U_{cal} values are 1305.0 and 1569.5 cm^{-1} for **2** and **3**, respectively. The presence of the electron-donating –CH_3 group (see the computed NPA charges in Table S6†) in the Cp* ligand and the relatively small bent angles increases the metal–ligand interaction (π-type), which results in a higher U_{cal} value for **3**. Interestingly, the calculated U_{cal} value of **3** is comparable to that of **1**, which possesses a dianionic $(C_4H_4)^{2-}$ ligand. The effects of π-type interactions are well captured by the AILFT[111] computed f-orbital splitting pattern, which displays a preferential destabilization of the f_{xz^2}/f_{yz^2} orbitals compared to other 4f orbitals. For complexes **1–3**, we observed the following splitting pattern $f_{xz^2}/f_{yz^2} > f_{z^3} > f_{z(x^2-y^2)}/f_{xyz} > f_{x(x^2-3y^2)}/f_{y(3x^2-y^2)}$, with relatively stronger splitting for **3** (see Fig. S1†), which indicates that the relatively large $\angle L_{cent}$–Dy–L_{cent} angle in **3** dramatically increases the axial ligand field splitting and takes precedence over the electrostatic effects provided by the dianionic $(C_4H_4)^{2-}$ ligand.

Next, we compared the single-ion magnetic properties of **2** and **3** with their non-bucky analogues $[DyCp_2]^+$ (**2a**) and $[DyCp^*_2]^+$ (**3a**) to assess the effect of bulky fullerenes. The first noticeable effect is witnessed in the structural parameters, where **2** (145°) and **3** (160°) show a larger $\angle L_{cent}$–Dy–L_{cent} angle than complexes **2a** (129°) and **3a** (148°), suggesting that the bulkiness offered by substituted fullerenes naturally offers more linearity (see Table S1†). For **2a**, the span of eight low-lying KDs and U_{cal} value is shrunk by 7.0% and 14.9%, respectively, compared to **2**, indicating a strong axial ligand field in **2**. A fair comparison can be made between **3** and **3a** where one of the X′ ligands is different. For **3a**, the U_{cal} values and the span of the eight low-lying KDs are 1551.5 cm^{-1} and 1668.5 cm^{-1}, respectively, nearly similar to what was observed for complex **3** (see Tables S11 and S12†). The similarity in the span of eight low-lying KDs hints that the strength of the ligand field is nearly similar for both **3** and **3a** despite having a larger $\angle L_{cent}$–Dy–L_{cent} angle in **3**. The only noticeable difference is observed in the computed k_{QTM} values, which are ~10× times smaller for complex **3** ($k_{QTM} = 6.55 \times 10^{-8}$) than **3a** ($k_{QTM} = 6.02 \times 10^{-7}$). To further understand the origin of similarity in the span of eight low-lying KDs, we investigated the electronic effects of ligands by analyzing CASSCF computed Mulliken charges. In complex **3a**, we observed that each Cp* ring carries a charge of ~−1.17 a.u, which is significantly higher compared to the −0.38 a.u charges on the coordinated five-membered ring of $(C_{55}(CCH_3)_5)^-$ ligand in **3** (see Fig. S2†). CASSCF computed Mulliken charge distribution in **3** resembles the DFT computed NPA charges (see Table S6 and Fig. S3†). Our charge analysis suggests that the abruption of π-conjugation by substituting α-carbons largely compensates the negative charges on the coordinated atoms of the five-member ring, leading to a weaker electrostatic field in the $(C_{55}(CCH_3)_5)^-$ ligand compared to Cp* ligands. Our previous work on organometallic sandwiched complexes suggests that electrostatic effects are much weaker than the structural parameters, and the $\angle L_{cent}$–Dy–L_{cent} angle is the critical parameter to attain giant U_{cal} value in these complexes.[29] Despite having a large $\angle L_{cent}$–Dy–L_{cent} angle in **3**, a relatively more electron-deficient five-membered ring of the $(C_{55}(CCH_3)_5)^-$ ligand compared to the Cp* ligand competes with the structural benefits, resulting in no substantial increase in the U_{cal} values compared to **3a**. Both electronic and structural effects oppose each other in complex **3** and **3a**, resulting in similar U_{cal} values (see Fig. S2†). Recent studies indicate that high-temperature magnetic relaxation in $[Dy(Cp^{ttt})_2]^+$ complexes is induced by Cp–H bending modes, where strong spin–vibronic coupling leads to faster relaxation despite having large U_{eff} values.[25,40,41,112] In this context, rigid frameworks offered by the substituted fullerene ligands offer a

way to reduce these vibrational motions, which in turn reduces the resonance between the vibronic and electronic states and, hence, pave the way to slower the magnetic relaxation in Dy(III) based exohedral complexes.

For complex **4**, we observed the stabilization of m_J $|\pm15/2\rangle$ as the ground state with Ising type anisotropy, g_{zz} = 19.976, g_{xx} = g_{yy} = 1 × 10^{-4}. Compared to complexes **3**(**2**), the energy span of eight KDs is narrowed by 28% (16%) for **4**, which arises due to the weak electrostatic interaction between the Dy(III) ion and the neutral C_6H_6 ring. For complex **4**, the magnetic relaxation occurs *via* the 7th excited KD, resulting in a U_{cal} value of 1124 cm^{-1} with an extremely weak ground state k_{QTM} value of 1.71 × $10^{-7}\mu_B$. As observed earlier,[29] the nature of Dy(III) and ligand interactions remains π-type with the following splitting pattern: $f_{xz^2}/f_{yz^2} > f_{z^3} > f_{z(x^2-y^2)}/f_{xyz} > f_{x(x^2-3y^2)}/f_{y(3x^2-y^2)}$, resulting in a high axiality in complex **4**, despite having the neutral C_6H_6 ligand (see Fig. S1†).

On the other hand, in complex **5**, the ligand field stabilizes m_J $|\pm9/2\rangle$ primarily as the ground state (39% $|\pm9/2\rangle$ + 27% $|\pm5/2\rangle$ + 15% $|\pm11/2\rangle$), which is strongly mixed with other KDs (see Table S15†). The computed ground state *g*-values are axial with a sizable transverse component (g_{zz} = 9.744, g_{xx} = 0.193, g_{yy} = 0.314), a typical manifestation of a low m_J state. As a result, we have noticed a giant k_{QTM} value of 1.71 × $10^{-2}\mu_B$ in complex **5**, which indicates strong QTM to be operative within the ground state. Analysis of the *g*-tensor orientation and blockade barrier predicts that the magnetic relaxation is likely to occur *via* the 6th KD through a thermally activated process, which sets the U_{cal} value of 108.4 cm^{-1}. Moreover, we observed the following orbital ordering, $f_{z(x^2-y^2)}/f_{xyz} > f_{x(x^2-3y^2)}/f_{y(3x^2-y^2)} > f_{xz^2}/f_{yz^2} > f_{z^2}$ in **5**, which differs from what we observed for complexes **1**–**4**. Although the $(C_8H_8)^{2-}$ ligand is dianionic, similar to the $(C_4H_4)^{2-}$ ligand in **1**, the large ring size of the $(C_8H_8)^{2-}$ ring changes the 4f-ligand bonding interaction from π-type to δ-type, which generates an unfavourable equatorial ligand field and stabilizes the m_J $|\pm9/2\rangle$ ground state.[29,113]

Next, we analyzed the magnetic anisotropy and SIM behaviour in complexes **6**–**8**, where the Dy(III) ion is sandwiched between two $(C_{55}X_5)^-$ ligands (where X = CCH_3, B, and N). DFT optimization predicts a perfect linear arrangement around the Dy(III) ion where both the $(C_{55}X_5)^-$ ligands are arranged in a staggered fashion (D_{5d}). As a result of the strict linearity around the Dy(III) ion in complexes **6**–**8**, we observed stabilization of pure m_J $|\pm15/2\rangle$ as the ground state with negligible mixing with other excited states. CASSCF computed *g*-values for complexes **6**–**8** are highly anisotropic in nature and show an Ising type feature (g_{xx} = g_{yy} ≈ 1 × 10^{-4} and g_{zz} = 19.998(**6**), g_{xx} = g_{yy} ≈ 1 × 10^{-4} and g_{zz} = 19.996(**7**) and g_{xx} = g_{yy} ≈ 1 × 10^{-4} and g_{zz} = 19.998(**8**)). The eight low-lying KDs span over an energy range of 1573.7, 1284.1, and 1347.0 cm^{-1} for complexes **6**–**8**, respectively. For complexes **6**–**8**, the principal *z*-axis of the *g*-tensor passes with the highest C_5 symmetry axis, which passes through the center of the attached $(C_{55}X_5)^-$ ligands. Due to higher order symmetry, the orientation of all eight KDs is perfectly collinear with each other, resulting in the magnetization blockade up to the 7th KD, which enables the magnetic relaxation *via* the 8th KD (m_J $|\pm1/2\rangle$). The computed U_{cal} values are the same as the energy span of low-lying KDs in the following order: U_{cal} (**6**) > U_{cal} (**8**) > U_{cal} (**7**), with the largest U_{cal} value reported for complex **6**. As the local structural parameters of complexes **6**–**8** are similar, the observed differences in U_{cal} might be due to the differences in the electronic effects. As observed in the EDA analysis, the accumulation of negative charges around the Cp ring and α-C atoms in **6** generates more electrostatic interaction from the axial direction, which helps to maximize the splitting of the $^6H_{15/2}$ state. In contrast, a relatively weaker ligand field is generated in complexes **7** and **8** where the α-C atoms are substituted by B and N atoms, resulting in relatively smaller U_{cal} values. The ground state transverse magnetic moment is 3.99 × $10^{-9}\mu_B$, 2.37 × $10^{-7}\mu_B$, and 8.99 × $10^{-8}\mu_B$ for complexes **6**, **7**, and **8**, respectively, indicating complete quenching of the QTM within the ground state. Our single-ion analysis suggests that all three complexes (**6**–**8**) are potentially good candidates for the isolation of Dy(III) based SIM; however, **6** shows an exceptionally giant barrier height and extremely weak ground state k_{QTM} values. The computed U_{cal} value of **6** is even more significant than the U_{cal} value observed for the $[DyCp^*_2]^+$ (**3a**) complex, which makes them highly promising for SMM designing. When comparing the k_{QTM} values of complex **3a** with complex **6**, we observed that the k_{QTM} value of **6** (k_{QTM} = 3.99 × $10^{-9}\mu_B$) is approximately 150× smaller than that of complex **3a** (k_{QTM} = 6.02 × $10^{-7}\mu_B$), which is attributed solely to the strict linearity found in complex **6**. The computed *ab initio* blockade barrier for complexes **6**–**8** is depicted in Fig. 6. Although the $(C_{55}X_5)^-$ (where X = CCH_3, N or B) ligands offer a relatively weak electrostatic field compared to the Cp* ligand, the strict linearity offered by the $(C_{55}(CCH_3)_5)^-$ ligand in complexes **6**–**8**, makes them promising candidates for designing new-generation of exohedral substituted fullerenes based organometallic Dy(III) SMMs.

Next, we computed the temperature-dependent effective demagnetization barrier (U_{eff}) and the relative contribution from each KD, which helped us to understand the Orbach relaxation (see Fig. 7, S4, and Table S16†). For all the studied complexes, we observed that the *ab initio* blockade barrier nicely matches the demagnetization barrier, indicating that all these complexes are highly symmetric and exhibit negligible QTM values. From 0 K to 300 K, the temperature dependence of both U_{eff} and the contributions from various KDs for complexes **1**–**8** is illustrated in Fig. 7 and S4.† The entire temperature range can be divided into three regions: (I) the initial temperature region, (II) the region where U_{eff} rises sharply, and (III) the region where U_{eff} saturates. Within region I, the U_{eff} remains nearly zero since all the populations are in the m_J $|\pm15/2\rangle$ ground state, which is blocked due to the minimal k_{QTM} value (~10^{-6}–$10^{-9}\mu_B$) except for complex **5** (~$10^{-2}\mu_B$). This region continues up to 50 K, which indicates that the QTM is completely blocked at this temperature, and other relaxation processes, such as Orbach/Raman relaxation, must be considered in this region. In region II, a rapid temperature increase causes a rapid population growth of other excited KDs. As temperature increases beyond 50 K, the U_{eff} value

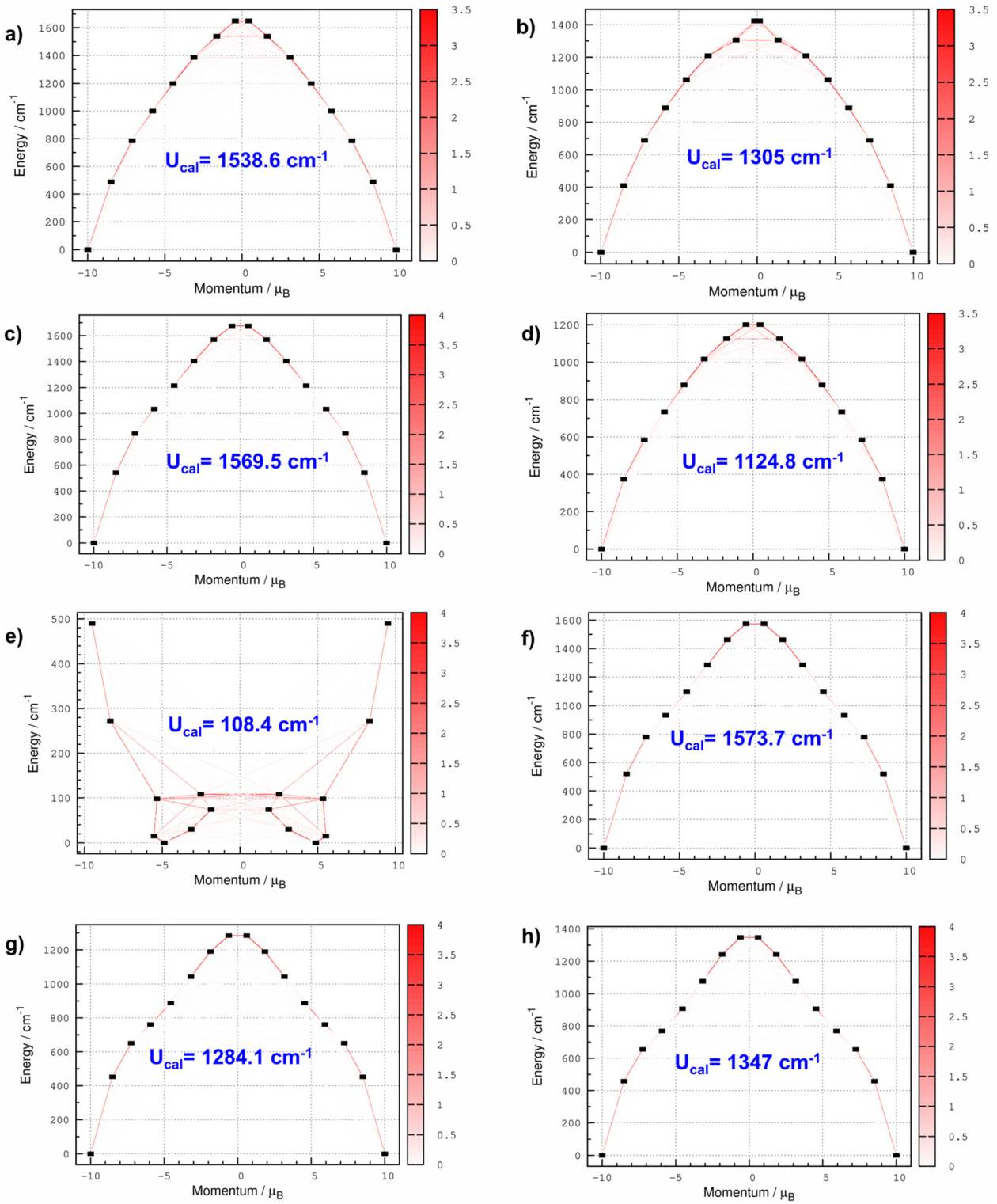

Fig. 6 (a)–(h) SINGLE_ANISO computed magnetization blockade barriers for complexes **1–8**, respectively.

increases by climbing to the higher excited KDs with sequential absorption of the thermally available phonons for all the complexes except **5**. In region III, U_{eff} saturates, and the Orbach regime is reached for all the complexes at room temperature. Among complexes **1–8**, complex **3** shows the largest U_{eff} value of 1627.5 cm^{-1}, while complex **5** shows the smallest U_{eff} value of ~95.2 cm^{-1}. We observed the following U_{eff} values: 1533 cm^{-1}, 1235 cm^{-1}, and 1314 cm^{-1} for complexes **6–8**,

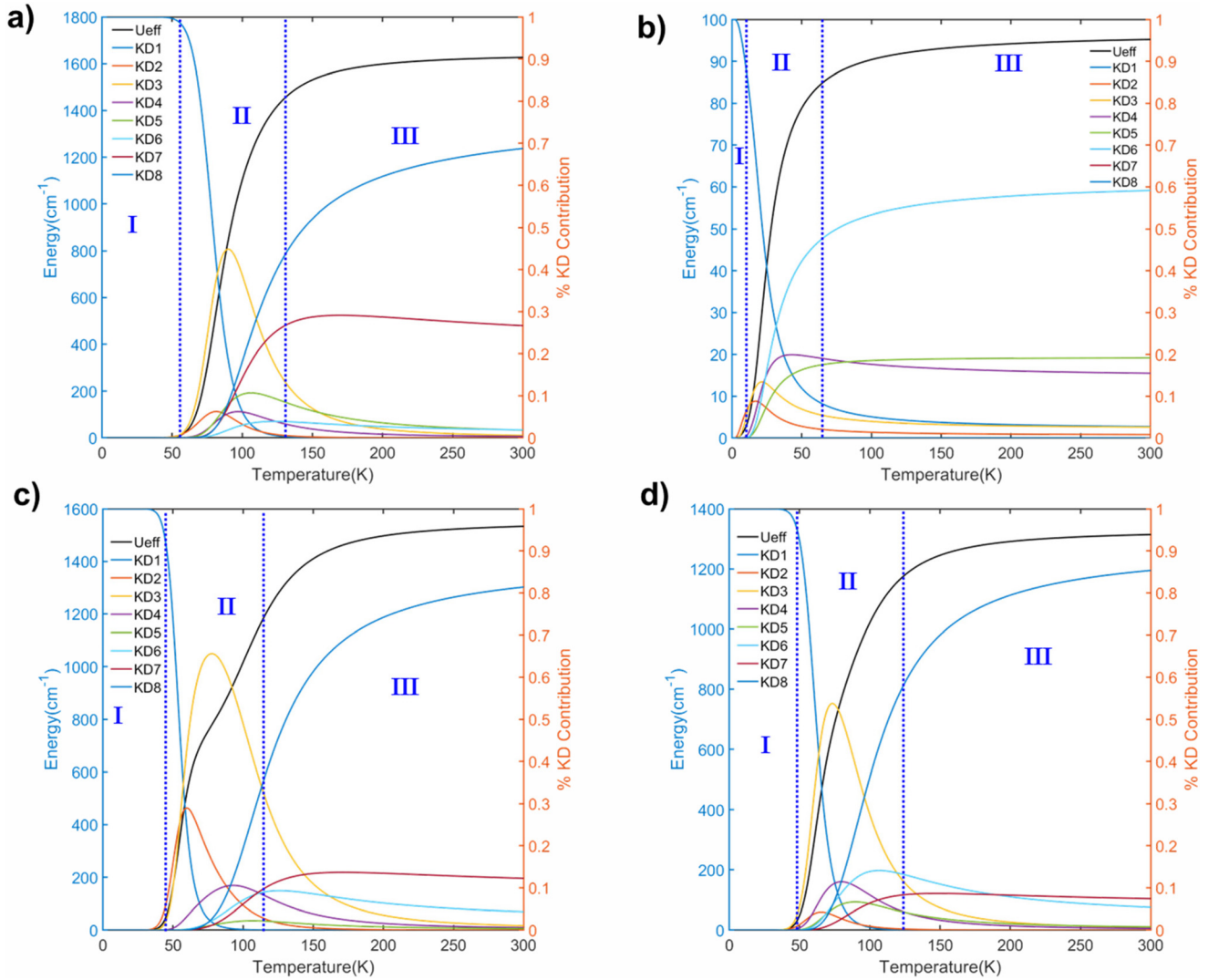

Fig. 7 Temperature dependence of calculated U_{eff}, along with the relative contribution of each Kramers doublet to the relaxation, calculated as $k_i(T)/N_k$ for (a) **3**, (b) **5**, (c) **6**, and (d) **8**.

respectively, which agrees with the trends observed from *ab initio* calculations. In complex **6**, the saturation in U_{eff} emerges from three KDs (KD8 81% + KD7 12% + KD6 4%) (see Table S16†), indicating that thermal-assisted quantum tunnelling of magnetization (TA-QTM) is completely blocked at lower KDs, a typical manifestation of ideal Dy(III) based SIM in complete axial ligand field. SINGLE_ANISO computed energy of KD8 is 1573.7 cm^{-1}, nearly the same as the saturated U_{eff} value of 1533 cm^{-1}. A careful analysis of temperature dependence data reveals a slight hump in region II of complex **6**, which might be due to the similar strength of k_{QTM} values of KD3 and KD4 (3.12×10^{-3} and 3.03×10^{-3}), indicating a probable path for thermally assisted QTM. The wave function decomposition analysis shows significant mixing between the KD3 (78.5% $|\pm 11/2\rangle$ + 17.5% $|\pm 9/2\rangle$) and KD4(77.6% $|\pm 9/2\rangle$ + 20% $|\pm 11/2\rangle$) which is the cause for the similar superposition of the k_{QTM} values. It is important to note that the computed U_{eff} and T_B values obtained from eqn (6) and (7) do not consider the Raman mechanism for magnetic relaxation. Hence, the computed U_{eff} and T_B values must be viewed as an upper limit as the presence of Raman relaxation can further lower U_{eff} and T_B significantly.[98]

Conclusion

To this end, for the first time, we have successfully explored the capability of substituted fullerenes as $(Cp)^-$ mimicking ligands towards stabilizing novel Dy(III) exohedral substituted fullerene complexes, which are relevant for designing a new generation of organometallic SIMs. DFT-optimized structural parameters reveal that complexes **1–4** possess a bent geometry while complexes **5–8** possess a linear geometry around the Dy(III) ion. The bulkiness of two $(C_{55}X_5)^-$ ligands leads to a strictly

linear geometry in complexes **6–8**, which is otherwise a non-trivial task to achieve by bulking the Cp ligand. Thermodynamic and interaction energy analysis at the SR-DFT level of theory predicts that these Dy(III) exohedral substituted fullerene complexes **1–8** are highly stable in nature. EDA analysis predicts stabilization in terms of interaction energy in the following order: **5** > **1** > **2** ≈ **3** > **6** > **7** > **8** > **4**, and the decomposed interaction energy suggests that both the electrostatic and orbital interactions are the most dominant contributors in all these complexes. The total interaction energy trend is consistent with the observed trend in ΔE_{elstat} values, suggesting that electrostatic interactions regulate the overall interaction energy. Among complexes **6–8**, where the Dy(III) ion is sandwiched between the two $(C_{55}X_5)^-$ ligands, the interaction energy is relatively weaker compared to that of $[DyCp^*_2]$ cations (**3a**), suggesting that the $(C_{55}X_5)^-$ ligands are relatively electron deficient compared to the Cp* ligands. NPA charge analysis and ETS-NOCV deformation density analysis predict a charge flow from the π-lobes of the ligands to 4f and vacant 5d orbitals of the Dy(III) ions, indicating the importance of both 4f/5d orbitals in bonding. Due to highly symmetric structures, CASSCF calculations predict the stabilization of m_J $|\pm 15/2\rangle$ as the ground state for all the complexes except for **5**, with the following trend in the U_{cal} values: **6** (1573 cm^{-1}) ≈ **3** (1569 cm^{-1}) > **1** (1538 cm^{-1}) > **8** (1347 cm^{-1}) > **2** (1305 cm^{-1}) > **7** (1284 cm^{-1}) > **4** (1125 cm^{-1}) > **5** (108 cm^{-1}). The π-type 4f-ligand interaction in complexes **1–4** helps to generate a giant axial ligand field, while the δ-type interaction between 4f and the $(C_8H_8)^{2-}$ ligand diminishes the axial ligand field and SMM behaviour. CASSCF calculations predict a giant magnetization barrier with strictly no QTM within the ground states (k_{QTM} = 10^{-7}–10^{-9}) for complexes **6–8**. Due to structural similarity in complexes **6–8**, the observed trend in the U_{cal} values is solely controlled by the ligand's electronic effects, which are nicely captured in the computed NPA charges and MEPs. Substitution at the α-carbon strongly affects the electronic properties of $(C_{55}X_5)^-$ (where X = CCH_3, B, and N) ligands, which is key in tuning the SIM behaviour in these complexes. Among the studied substituted fullerene ligands, the sp^3 hybridized α-C carbon in the $(C_{55}(CCH_3)_5)^-$ ring makes the five-membered ring electron-rich compared to B/N analogues which significantly increases the barrier height in **6** compared to those in **7** and **8**. Effective demagnetization barrier analysis clearly shows that U_{eff} is zero below 50 K for all the complexes with the dominant contribution arising from the KD8, highlighting that highly symmetric environments completely quench the TA-QTM at lower KDs and allow Orbach relaxation to take place *via* the highest KD in all the complexes. Replacing Cp* with $(C_{55}X_5)^-$ ligands offers a viable way to isolate stable linear exohedral Dy(III) organometallic sandwiched complexes with U_{cal} exceeding 1500 cm^{-1}, which is close to the values reported for $[DyCp^*_2]^+$ cations. Our detailed findings predict substituted fullerenes as promising capping ligands for designing the next generation of stable linear Dy(III) based exohedral single-ion magnets displaying giant barrier height with negligible QTM in the ground state.

Data availability

The data supporting this article have been included as part of the ESI.†

Conflicts of interest

There are no conflicts to declare.

Acknowledgements

SKS acknowledges the Science and Engineering Research Board (CRG/2023/002936) and IIT Hyderabad for generous funding. KK acknowledges PMRF. SKS and KK acknowledge PARAM Seva Computing Facility under the National Supercomputing Mission at IIT Hyderabad.

References

1 D. N. Woodruff, R. E. P. Winpenny and R. A. Layfield, *Chem. Rev.*, 2013, **113**, 5110–5148.
2 J. Lu, M. Guo and J. Tang, *Chem. – Asian J.*, 2017, **12**, 2772–2779.
3 A. Z. Lekuona, J. M. Seco and E. Colacio, *Coord. Chem. Rev.*, 2021, **441**, 213984.
4 J. L. Liu, Y. C. Chen and M. L. Tong, *Chem. Soc. Rev.*, 2018, **47**, 2431–2453.
5 N. F. Chilton, *Inorg. Chem.*, 2015, **54**, 2097–2099.
6 Y. S. Ding, Y. F. Deng and Y. Z. Zheng, *Magnetochemistry*, 2016, **2**, 40.
7 M. Shiddiq, D. Komijani, Y. Duan, A. G. Ariño, E. Coronado and S. Hill, *Nature*, 2016, **531**, 348–351.
8 R. E. P. Winpenny, *Angew. Chem., Int. Ed.*, 2008, **47**, 7992–7994.
9 A. Candini, S. Klyatskaya, M. Ruben, W. Wernsdorfer and M. Affronte, *Nano Lett.*, 2011, **11**, 2634–2639.
10 M. N. Leuenberger and D. Loss, *Nature*, 2001, **410**, 789–793.
11 A. G. Ariño, F. Luis, S. Hill and E. Coronado, *Nat. Chem.*, 2019, **11**, 301–309.
12 A. Ardavan and S. J. Blundell, *J. Mater. Chem.*, 2009, **19**, 1754–1760.
13 L. Bogani and W. Wernsdorfer, *Nat. Mater.*, 2008, **7**, 179–186.
14 R. Vincent, S. Klyatskaya, M. Ruben, W. Wernsdorfer and F. Balestro, *Nature*, 2012, **488**, 357–360.
15 S. G. Coca, E. Cremades, N. A. Alcalde and E. Ruiz, *J. Am. Chem. Soc.*, 2013, **135**, 7010–7018.
16 E. Ruiz, J. Cirera, J. Cano, S. Alvarez, C. Loose and J. Kortus, *Chem. Commun.*, 2007, 52–54.
17 S. G. Coca, D. Aravena, R. Morales and E. Ruiz, *Coord. Chem. Rev.*, 2015, , **289–290**, 379–392.

18 F. S. Guo, B. M. Day, Y. C. Chen, M. L. Tong, A. Mansikkamäki and R. A. Layfield, *Science*, 2018, **362**, 1400–1403.
19 L. Ungur, J. J. Le Roy, I. Korobkov, M. Murugesu and L. F. Chibotaru, *Angew. Chem., Int. Ed.*, 2014, **53**, 4413–4417.
20 P. Zhang, L. Zhang, C. Wang, S. Xue, S.-Y. Lin and J. Tang, *J. Am. Chem. Soc.*, 2014, **136**, 4484–4487.
21 M. Li, J. Han, H. Wu, Y. Du, Y. Liu, Y. Chen and S. Chen, *Dalton Trans.*, 2022, **51**, 16964–16972.
22 S. Moorthy, I. Tarannum, K. Kumari and S. K. Singh, *Dalton Trans.*, 2024, **53**, 12073–12079.
23 J. D. Rinehart and J. R. Long, *Chem. Sci.*, 2011, **2**, 2078.
24 S. Lee and T. Ogawa, *Chem. Lett.*, 2017, **46**, 10–18.
25 C. A. P. Goodwin, F. Ortu, D. Reta, N. F. Chilton and D. P. Mills, *Nature*, 2017, **548**, 439–442.
26 A. H. Vincent, Y. L. Whyatt, N. F. Chilton and J. R. Long, *J. Am. Chem. Soc.*, 2023, **145**, 1572–1579.
27 J. C. Vanjak, B. O. Wilkins, V. Vieru, N. S. Bhuvanesh, J. H. Reibenspies, C. D. Martin, L. F. Chibotaru and M. Nippe, *J. Am. Chem. Soc.*, 2022, **144**, 17743–17747.
28 F. S. Guo, M. He, G. Z. Huang, S. R. Giblin, D. Billington, F. W. Heinemann, M. L. Tong, A. Mansikkamäki and R. A. Layfield, *Inorg. Chem.*, 2022, **61**, 6017–6025.
29 I. Tarannum, S. Moorthy and S. K. Singh, *Dalton Trans.*, 2023, **52**, 15576–15589.
30 J. P. Durrant, B. M. Day, J. Tang, A. Mansikkamäki and R. A. Layfield, *Angew. Chem.*, 2022, **134**, e202200525.
31 J. Acharya, N. Ahmed, J. F. Gonzalez, P. Kumar, O. Cador, S. K. Singh, F. Pointillart and V. Chandrasekhar, *Dalton Trans.*, 2020, **49**, 13110–13122.
32 P. Kalita, N. Ahmed, S. Moorthy, V. Béreau, A. K. Bar, P. Kumar, P. Nayak, J.-P. Sutter, S. K. Singh and V. Chandrasekhar, *Dalton Trans.*, 2023, **52**, 2804–2815.
33 A. B. Canaj, S. Dey, C. Wilson, O. Céspedes, G. Rajaraman and M. Murrie, *Chem. Commun.*, 2020, **56**, 12037–12040.
34 Y. C. Chen, J. L. Liu, L. Ungur, J. Liu, Q. W. Li, L. F. Wang, Z. P. Ni, L. F. Chibotaru, X. M. Chen and M. L. Tong, *J. Am. Chem. Soc.*, 2016, **138**, 2829–2837.
35 S. Bala, G. Z. Huang, Z. Y. Ruan, S. G. Wu, Y. Liu, L. F. Wang, J. L. Liu and M. L. Tong, *Chem. Commun.*, 2019, **55**, 9939–9942.
36 A. B. Canaj, S. Dey, E. R. Martí, C. Wilson, G. Rajaraman and M. Murrie, *Angew. Chem., Int. Ed.*, 2019, **58**, 14146–14151.
37 M. Tricoire, L. Münzfeld, J. Moutet, N. Mahieu, L. La Droitte, E. Moreno-Pineda, F. Gendron, J. D. Hilgar, J. D. Rinehart, M. Ruben, B. Le Guennic, O. Cador, P. W. Roesky and G. Nocton, *Chem. – Eur. J.*, 2021, **27**, 13558–13567.
38 M. D. Korzyński, M. Bernhardt, V. Romankov, J. Dreiser, G. Matmon, F. Pointillart, B. L. Guennic, O. Cador and C. Copéret, *Chem. Sci.*, 2022, **13**, 10574–10580.
39 M. Jeletic, P.-H. Lin, J. J. Le Roy, I. Korobkov, S. I. Gorelsky and M. Murugesu, *J. Am. Chem. Soc.*, 2011, **133**, 19286–19289.
40 D. Reta, J. G. C. Kragskow and N. F. Chilton, *J. Am. Chem. Soc.*, 2021, **143**, 5943–5950.
41 A. Mattioni, J. K. Staab, W. J. A. Blackmore, D. Reta, J. Iles-Smith, A. Nazir and N. F. Chilton, *Nat. Commun.*, 2024, **15**, 485.
42 A. A. Popov, S. Yang and L. Dunsch, *Chem. Rev.*, 2013, **113**, 5989–6113.
43 L. Spree and A. A. Popov, *Dalton Trans.*, 2019, **48**, 2861–2871.
44 M. Toganoh, Y. Matsuo and E. Nakamura, *J. Am. Chem. Soc.*, 2003, **125**, 13974–13975.
45 E. D. Jemmis, M. Manoharan and P. K. Sharma, *Organometallics*, 2000, **19**, 1879–1887.
46 L. Zhu, T. Zhang, M. Yi and J. Wang, *J. Phys. Chem. A*, 2010, **114**, 9398–9403.
47 S. Hokmi, S. Salehzadeh and Y. Gholiee, *J. Comput. Chem.*, 2021, **42**, 1354–1363.
48 S. Anila and C. H. Suresh, *Phys. Chem. Chem. Phys.*, 2021, **23**, 3646–3655.
49 L. Dunsch, S. Yang, L. Zhang, A. Svitova, S. Oswald and A. A. Popov, *J. Am. Chem. Soc.*, 2010, **132**, 5413–5421.
50 W. Xiang, X. Jiang, Y. R. Yao, J. Xin, H. Jin, R. Guan, Q. Zhang, M. Chen, S. Y. Xie, A. A. Popov and S. Yang, *J. Am. Chem. Soc.*, 2022, **144**, 21587–21595.
51 Y. Shen, X. Yu, Q. Meng, Y. R. Yao, J. Autschbach and N. Chen, *Chem. Sci.*, 2022, **13**, 12980–12986.
52 X. Zhang, W. Li, L. Feng, X. Chen, A. Hansen, S. Grimme, S. Fortier, D. C. Sergentu, T. J. Duignan, J. Autschbach, S. Wang, Y. Wang, G. Velkos, A. A. Popov, N. Aghdassi, S. Duhm, X. Li, J. Li, L. Echegoyen, W. H. E. Schwarz and N. Chen, *Nat. Commun.*, 2018, **9**, 2753.
53 J. Zhuang, L. Abella, D. C. Sergentu, Y. R. Yao, M. Jin, W. Yang, X. Zhang, X. Li, D. Zhang, Y. Zhao, X. Li, S. Wang, L. Echegoyen, J. Autschbach and N. Chen, *J. Am. Chem. Soc.*, 2019, **141**, 20249–20260.
54 A. A. Popov and L. Dunsch, *J. Am. Chem. Soc.*, 2007, **129**, 11835–11849.
55 F. Liu, D. S. Krylov, L. Spree, S. M. Avdoshenko, N. A. Samoylova, M. Rosenkranz, A. Kostanyan, T. Greber, A. U. B. Wolter, B. Büchner and A. A. Popov, *Nat. Commun.*, 2017, **8**, 16098.
56 A. A. Popov and L. Dunsch, *Chem. – Eur. J.*, 2009, **15**, 9707–9729.
57 G. Velkos, W. Yang, Y.-R. Yao, S. M. Sudarkova, F. Liu, S. M. Avdoshenko, N. Chen and A. A. Popov, *Chem. Commun.*, 2022, **58**, 7164–7167.
58 M. K. Singh and G. Rajaraman, *Chem. Commun.*, 2016, **52**, 14047–14050.
59 M. K. Singh, P. Shukla, M. Khatua and G. Rajaraman, *Chem. – Eur. J.*, 2020, **26**, 464–477.
60 S. Dey and G. Rajaraman, *Chem. Sci.*, 2021, **12**, 14207–14216.
61 P. W. Fowler and A. Ceulemans, *J. Phys. Chem.*, 1995, **99**, 508–510.
62 A. L. Balch and M. M. Olmstead, *Chem. Rev.*, 1998, **98**, 2123–2166.

63 Y. Matsuo, Y. Kuninobu, S. Ito and E. Nakamura, *Chem. Lett.*, 2004, **33**, 68–69.
64 M. Sawamura, Y. Kuninobu, M. Toganoh, Y. Matsuo, M. Yamanaka and E. Nakamura, *J. Am. Chem. Soc.*, 2002, **124**, 9354–9355.
65 S. Hokmi, S. Salehzadeh and Y. Gholiee, *New J. Chem.*, 2022, **46**, 2678–2686.
66 J. Suzumura, N. Hosoya, S. Nagao, M. Mitsui and A. Nakajima, *J. Chem. Phys.*, 2004, **121**, 2649–2654.
67 S. Nagao, Y. Negishi, A. Kato, Y. Nakamura, A. Nakajima and K. Kaya, *J. Phys. Chem. A*, 1999, **103**, 8909–8914.
68 T. Sharma, M. K. Singh, R. Gupta, M. Khatua and G. Rajaraman, *Chem. Sci.*, 2021, **12**, 11506–11514.
69 E. Nakamura, *J. Organomet. Chem.*, 2004, **689**, 4630–4635.
70 D. Aravena, *J. Phys. Chem. Lett.*, 2018, **9**, 5327–5333.
71 A. Lunghi, F. Totti, R. Sessoli and S. Sanvito, *Nat. Commun.*, 2017, **8**, 14620.
72 A. Lunghi, F. Totti, S. Sanvito and R. Sessoli, *Chem. Sci.*, 2017, **8**, 6051–6059.
73 A. Lunghi and S. Sanvito, *Sci. Adv.*, 2019, **5**, eaax7163.
74 Y. C. Liu, Y. H. Kan, S. X. Wu, G. C. Yang, L. Zhao, M. Zhang, W. Guan and Z. M. Su, *J. Phys. Chem. A*, 2008, **112**, 8086–8092.
75 L. Zhao, M. von Hopffgarten, D. M. Andrada and G. Frenking, *Wiley Interdiscip. Rev.: Comput. Mol. Sci.*, 2018, **8**, e1345.
76 F. C. Guzmán and R. F. W. Bader, *Coord. Chem. Rev.*, 2005, **249**, 633–662.
77 F. Neese, F. Wennmohs, U. Becker and C. Riplinger, *J. Chem. Phys.*, 2020, **152**, 224108.
78 F. Neese, *Wiley Interdiscip. Rev.: Comput. Mol. Sci.*, 2022, **12**, e1606.
79 T. Nakajima and K. Hirao, *Chem. Rev.*, 2012, **112**, 385–402.
80 D. A. Pantazis and F. Neese, *J. Chem. Theory Comput.*, 2009, **5**, 2229–2238.
81 F. Weigend and R. Ahlrichs, *Phys. Chem. Chem. Phys.*, 2005, **7**, 3297–3305.
82 S. Grimme, S. Ehrlich and L. Goerigk, *J. Comput. Chem.*, 2011, **32**, 1456–1465.
83 S. Grimme, J. Antony, S. Ehrlich and H. Krieg, *J. Chem. Phys.*, 2010, **132**, 154104.
84 S. K. Singh, J. Eng, M. Atanasov and F. Neese, *Coord. Chem. Rev.*, 2017, **344**, 2–5.
85 M. Betzinger, C. Friedrich and S. Blügel, *Phys. Rev. B: Condens. Matter Mater. Phys.*, 2010, **81**, 195117.
86 G. te Velde, F. M. Bickelhaupt, E. J. Baerends, C. Fonseca Guerra, S. J. A. van Gisbergen, J. G. Snijders and T. Ziegler, *J. Comput. Chem.*, 2001, **22**, 931–967.
87 E. Van Lenthe and E. J. Baerends, *J. Comput. Chem.*, 2003, **24**, 1142–1156.
88 M. A. Watson, N. C. Handy and A. J. Cohen, *J. Chem. Phys.*, 2003, **119**, 6475–6481.
89 E. V. Lenthe, E. J. Baerends and J. G. Snijders, *J. Chem. Phys.*, 1994, **101**, 9783–9792.
90 B. O. Roos, P. R. Taylor and P. E. M. Sigbahn, *Chem. Phys.*, 1980, **48**, 157–173.
91 K. Bernot, J. Luzon, L. Bogani, M. Etienne, C. Sangregorio, M. Shanmugam, A. Caneschi, R. Sessoli and D. Gatteschi, *J. Am. Chem. Soc.*, 2009, **131**, 5573–5579.
92 G. Cucinotta, M. Perfetti, J. Luzon, M. Etienne, P.-E. Car, A. Caneschi, G. Calvez, K. Bernot and R. Sessoli, *Angew. Chem., Int. Ed.*, 2012, **51**, 1606–1610.
93 M. Briganti, G. F. Garcia, J. Jung, R. Sessoli, B. L. Guennic and F. Totti, *Chem. Sci.*, 2019, **10**, 7233–7245.
94 M. S. Norre, C. Gao, S. Dey, S. K. Gupta, A. Borah, R. Murugavel, G. Rajaraman and J. Overgaard, *Inorg. Chem.*, 2020, **59**, 717–729.
95 P. Kalita, K. Kumari, P. Kumar, V. Kumar, S. K. Singh, G. Rogez and V. Chandrasekhar, *Dalton Trans.*, 2024, **53**, 10521–10535.
96 D. Shao, W. J. Tang, Z. Ruan, X. Yang, L. Shi, X. Q. Wei, Z. Tian, K. Kumari and S. K. Singh, *Inorg. Chem. Front.*, 2022, **9**, 6147–6157.
97 L. F. Chibotaru and L. Ungur, *J. Chem. Phys.*, 2012, **137**, 064112.
98 A. C. Alvarez, Y. Gil, L. Llanos and D. Aravena, *Inorg. Chem. Front.*, 2020, **7**, 2478–2486.
99 S. D. Jiang, S. S. Liu, L. N. Zhou, B. W. Wang, Z. M. Wang and S. Gao, *Inorg. Chem.*, 2012, **51**, 3079–3087.
100 A. C. Parambil and A. Mansikkamäki, *J. Organomet. Chem.*, 2024, **1007**, 123024.
101 M. Mitoraj and A. Michalak, *J. Mol. Model.*, 2007, **13**, 347–355.
102 E. R. Johnson, S. Keinan, P. M. Sánchez, J. C. García, A. J. Cohen and W. Yang, *J. Am. Chem. Soc.*, 2010, **132**, 6498–6506.
103 A. Otero-de-la-Roza, E. R. Johnson and J. C. García, *Phys. Chem. Chem. Phys.*, 2012, **14**, 12165–12172.
104 T. Lu and F. Chen, *J. Comput. Chem.*, 2012, **33**, 580–592.
105 W. Humphrey, A. Dalke and K. Schulten, *J. Mol. Graph.*, 1996, **14**, 33–38.
106 R. F. Bader, *Acc. Chem. Res.*, 1985, **18**, 9–15.
107 M. Ziółkowski, S. J. Grabowski and J. Leszczynski, *J. Phys. Chem. A*, 2006, **110**, 6514–6521.
108 D. Cremer and E. Kraka, *Angew. Chem., Int. Ed. Engl.*, 1984, **23**, 627–628.
109 N. Kaltsoyannis, *Inorg. Chem.*, 2013, **52**, 3407–3413.
110 S. Cooper and N. Kaltsoyannis, *Dalton Trans.*, 2021, **50**, 1478–1485.
111 J. Jung, M. Atanasov and F. Neese, *Inorg. Chem.*, 2017, **56**, 8802–8816.
112 S. Dey, T. Sharma and G. Rajaraman, *Chem. Sci.*, 2024, **15**, 6465–6477.
113 K. R. Meihaus and J. R. Long, *J. Am. Chem. Soc.*, 2013, **135**, 17952–17957.